FINAL TECHNICAL REPORT

HIGH-RESOLUTION GEOPHYSICAL AND GEOLOGICAL INVESTIGATION OF LATE QUATERNARY DEFORMATION IN THE LOWER WABASH VALLEY FAULT ZONE

Award Number: 04HQGR0094

Principal Investigator: Edward W. Woolery

University of Kentucky
Department of Geological Sciences/
Kentucky Geological Survey
101 Slone Research Building
Lexington, KY 40506-0053
Phone: 859.257.3016
Fax: 859.323.1938
Email: woolery@uky.edu
http://www.uky.edu/AS/Geology/

Co-Investigator: Frederick A. Rutledge

University of Kentucky
Dept. of Geological Sciences
Lexington, KY 40506-0107
alexrutledge@gmail.com

Co-Investigator: Roy B. VanArsdale

University of Memphis
Department of Earth Sciences
Memphis, TN 38152-3430
Email: rvanrsdl@memphis.edu
Phone: 901.678.4356

Program Element: CU/I

Key Words: Neotectonics, Quaternary Fault Behavior, Reflection Seismology

The views and conclusions contained in this document are those of the authors and should not be interpreted as necessarily representing the official policies, either expressed or implied, of the U.S. Government.

Award Number: 04HQGR0094

HIGH-RESOLUTION GEOPHYSICAL AND GEOLOGICAL INVESTIGATION OF LATE QUATERNARY DEFORMATION IN THE LOWER WABASH VALLEY FAULT ZONE

Edward W. Woolery, *Dept. of Geological Sciences, University of Kentucky, 101 Slone Bldg., Lexington, Ky. 40506, Tel: 859.257.3016, Fax: 859.257.1147, Email: woolery@uky.edu*,

ABSTRACT

In order to better define the spatial and temporal characteristics of recently discovered neotectonic structure, approximately eight kilometers of SH-wave seismic reflection profiles were collected across the Mt. Vernon graben, a 35 km by 3 km graben (bounded by the Wabash Island (WIF) and Hovey Lake faults (HLF)) in the southern Wabash Valley fault system (WVFS) of southern Indiana. Although several anomalies were interpreted to affect Quaternary sediment, one of the more prominent was associated with the HLF. Consequently, this area was selected for our more focused field efforts. One kilometer of ground-penetrating radar data were subsequently collected across the primary HLF anomaly. In addition to the geophysical surveys, field investigations integrated reconnaissance geotechnical boreholes in the larger area, as well as 17 shallow continuous cores across the primary HLF anomaly. The drilling assisted with stratigraphic correlation and organic sampling for 14C age estimates.

The structural styles associated with the faults include: 1) normal displacement, 2) reverse displacement and other compressional features, 3) varying magnitudes of slip along fault planes, and 4) different senses of slip along individual fault planes. Carbon 14 dating of displaced horizons suggests movement between approximately 26,000 and 42,000 YBP. One sample taken from a deformed HLF horizon 1.2 m below ground surface suggested a 14C age of 1,100 YBP; however, this sample was not constrained well enough to eliminate the potential for post-depositional emplacement.

The style and timing of Quaternary deformation, the spatial correlation of Quaternary faults to documented Paleozoic bedrock faults, and focal mechanism studies of local seismicity suggest that the extensional genesis of the WVFS have been transpressionally reactivated: a manner consistent with an east-northeast–west-southwest-oriented regional compressive stress.

NONTECHNICAL SUMMARY

Subsurface geophysical images and correlative drilling within the southern Wabash Valley have provided evidence for tectonic activity during the Quaternary. The images, along with carbon-14 age measurements derived from organic samples collected from our drilling activities, have enabled us to approximate the time of movement and understand the style and geometry of the deformation. Results have shown that deformation extends to within at least 2 meters of the ground surface. The most reliable age estimates suggest that an upper bound for fault movement ranges between 26,000 and 42,000 BP. There are limitations to the resolving power of each geophysical and geological exploration technique used; consequently, the exact timing of the latest tectonic episode remains unknown. We hope to coordinate with, and provide target information to, researchers specializing in paleoseismologic trenching in order to reduce the uncertainty. Our results have design implications for high-hazard and critical facilities in the area. In addition, the findings also contribute to the USGS-NEHRP central U.S. efforts to locate/characterize seismogenic faults in order to better constrain seismic source zone boundaries.

INTRODUCTION

The Wabash Valley fault system (WVFS) is a linear, northeast–southwest-trending band of narrow graben structures that lies in the Wabash River valley of southern Indiana and Illinois (Fig. 1) (Bristol and Treworgy 1979; Treworgy, 1981; Ault and Sullivan, 1982; Ault et al., 1985; Rene and Stanonis, 1995). Paleoseismological evidence, historical earthquake accounts, and contemporary earthquake records also indicate that the Wabash Valley has a significant seismic hazard (e.g., Street et al., 1980; Obermeier et al., 1991; Pond and Martin, 1997; Munson et al., 1997; Pavlis et al., 2002; Kim, 2003). The pre-instrumental and instrumental evidence has shown that small to moderate earthquakes occur in an area roughly coincident with the WVFS (Fig. 2). The lower rate of seismicity, relative to the central New Madrid seismic zone, and insufficient seismic network coverage have made correlating seismicity with geological structure problematic, however. Consequently, eleven shallow shear-wave reflection surveys, totaling approximately 8 km in length, were acquired across the Mt. Vernon graben, a prominent well-defined Paleozoic structure that is bounded by the Wabash Island (WIF) and Hovey Lake (HLF) faults, to consider potential neotectonism (Fig. 3). The objective of the reflection surveys addressed two questions: (1) do the older geologic structures exhibit neotectonism that extends into the Quaternary cover, and (2) if neotectonic deformation is present, can dateable materials be recovered from the disrupted horizons to provide an age constraint for the fault activation? Subsequently, 1 km of ground-penetrating radar data were collected, as well as the drilling of 15 continuously sampled holes in order to better define the extent of the near-surface anomalies.

GEOLOGICAL AND SEISMOLOGICAL SETTING

The faults that comprise the lower WVFS were initially recognized during petroleum exploration drilling in the early part of the last century (Fig. 1). Since then, continued drilling and deep geophysical imaging have characterized the fault system as a series of high-angle, normal faults that are rooted in a series of basement-penetrating faults at seismogenic depths (Sexton et al., 1986; Rene and Stanonis, 1995; Bear et al., 1997). McBride et al. (1997) interpreted industry lines to show that the Paleozoic faults did not penetrate basement rocks west of the Inman East fault (Fig. 1). Scientific consensus is also lacking (e.g., Braile et al. 1982, 1986, 1997; Bear et al., 1997; Hildenbrand and Ravat, 1997) regarding the complex seismotectonic relationship of

the WVFS to other major regional geologic structures that exhibit both aseismic (i.e., Rough Creek Fault Zone) and seismic (i.e., Reelfoot Rift) characteristics (Fig. 1).

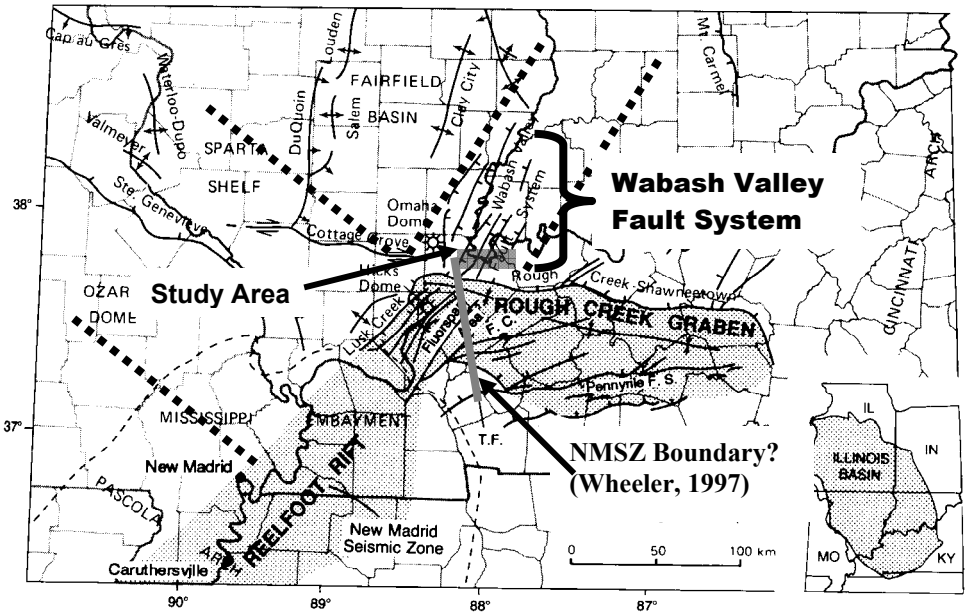

Figure 1. Regional structural features in the central U.S. (modified from Kolata and Hildebrand, 1997) and inferred quadruple junction (heavy dashed line) from Braile et al. (1986). The study area is shown as the heavy shaded area in the lowermost part of the Wabash Valley.

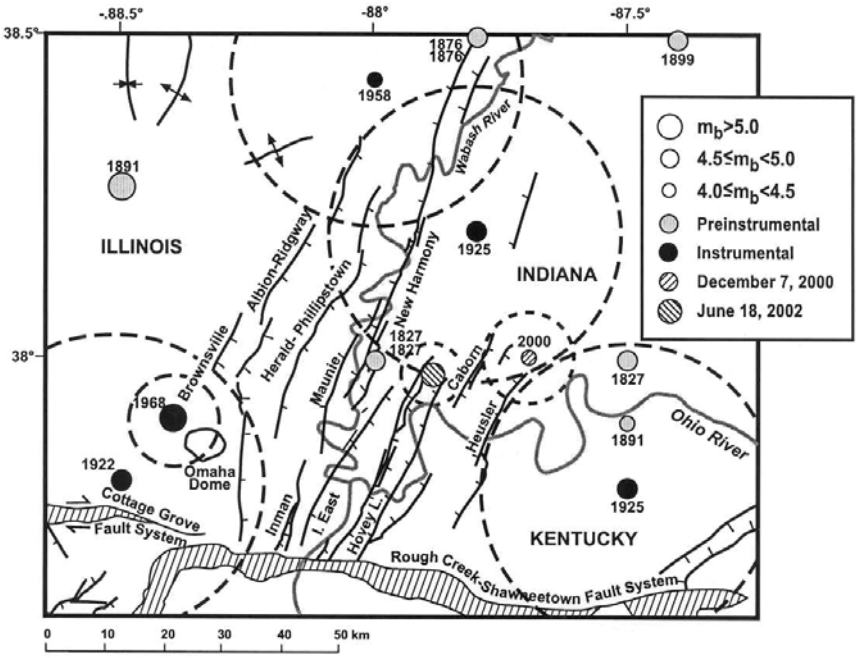

Figure 2. Location map that shows approximate location of historical and contemporary earthquakes in relationship to WVFS (modified from Bear et al., 1997 and Street et al., 2002). Dashed circles indicate uncertainty from instrumentally derived epicenters (filled circles). Shaded circles represent historical epicenters from individual investigators' interpretation of intensity reports.

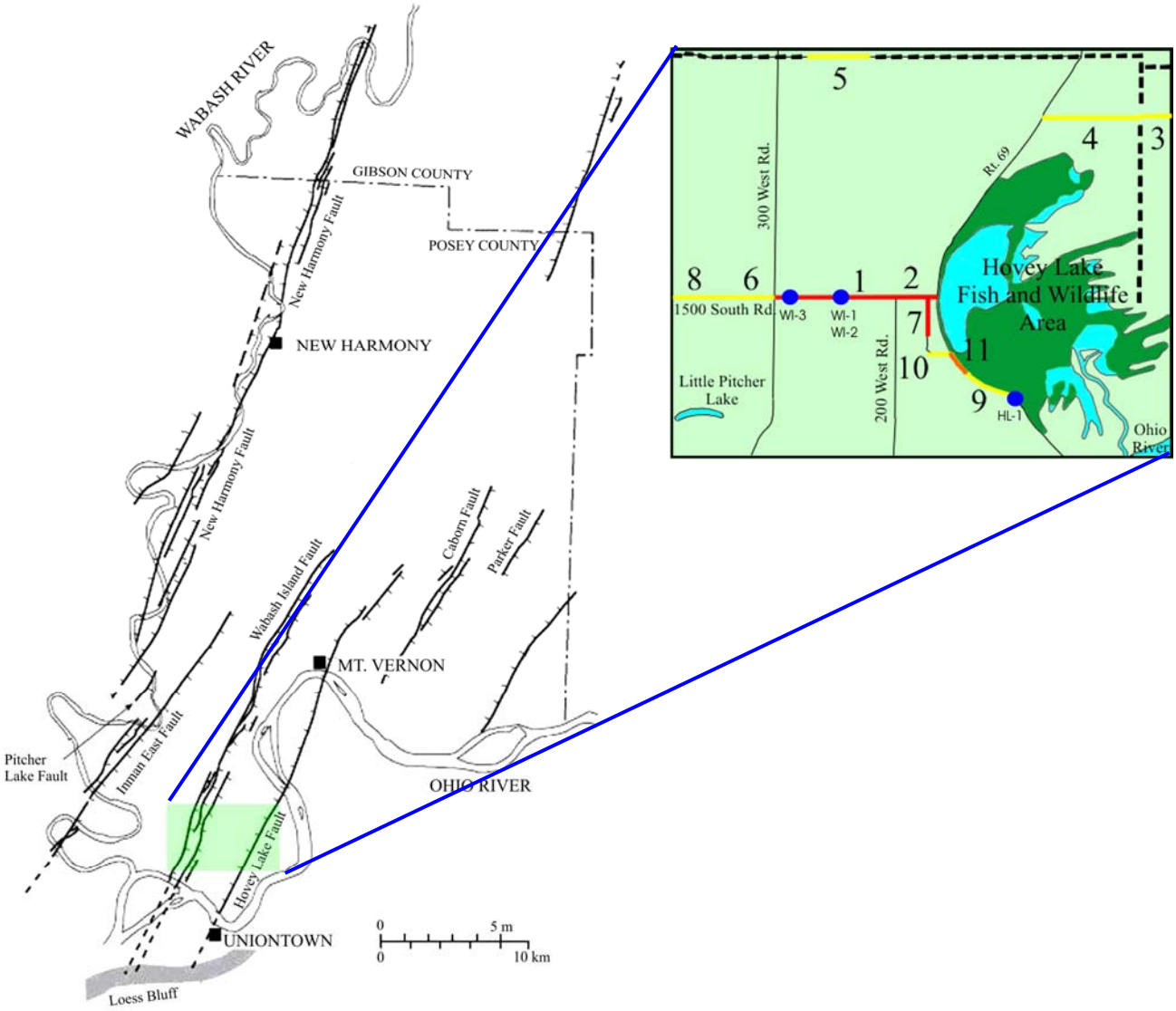

Figure 3. The light green shaded rectangle represents the approximate boundary of the study area. The inset map shows the 11 seismic surveys that total approximately 8 km in length. The orange line represents data collected at a 1-m group interval, the red lines represent a 2-m group interval, and the yellow lines represent a 4-m group interval. Numbers represent line number. The blue circles represent the reconnaissance geotechnical borehole locations of WI-1, WI-2, WI-3, and HL-1. Eleven follow-up borings were concentrated over the Quaternary anomalies marked by Line 11. The black dashed lines are the locations of deeper seismic-reflection profiles that imaged the Hovey Lake and Wabash Island faults at depth (Rene and Stanonis, 1995).

Despite these controversies, researchers agree that the southern halves of Indiana and Illinois are exposed to a significant level of earthquake hazard (Wheeler, 1997). Widespread Holocene paleoliquefaction features (Obermeier et al., 1991; Munson et al., 1997), as well as numerous small to moderate historical and contemporary seismic events during the past 200 years (Street et

al., 1980; Pavlis et al., 2002; Kim 2003) support this notion (Fig. 2). The largest event to have occurred since regional seismic networks were established was the 09 November 1968 magnitude 5.5 ($m_{b,Lg}$) earthquake, located near McBride et al.'s (1997) deep seismic profile, and approximately along the WVFS's southwestern boundary (Fig. 2). He presented convincing evidence that this earthquake was associated with a blind thrust fault in crystalline basement. The most recent earthquakes of significance are the magnitude 3.9 (m_b) event that occurred on 07 December 2000 near the Heusner fault, and the magnitude 5.0 (m_b) earthquake of 18 June 2002 that was located in close proximity to the Caborn and Hovey Lake faults (Fig. 2). Kim (2003) described the source mechanism for the 18 June 2002 event as predominantly strike-slip along near-vertical nodal planes, and suggested a seismogenic relationship to the Caborn fault. The northeast-oriented nodal plane is coincident with the regional strike of the WVFS.

The bedrock in the study area consists of predominantly Pennsylvanian sandstone, shale, coal (with clays), and occasional interbedded carbonates. Johnson and Norris (1976) reported that as much as 45 m of unlithified Quaternary alluvial and lacustrine sediment overlies the bedrock. They also stated that the sediment overburden generally consists of Pleistocene to Holocene clays underlain by a fining-upward sand sequence. Our four continuously sampled reconnaissance boreholes in the immediate area corroborate this stratigraphy (Fig. 3). The depth to bedrock (shale) measured in three boreholes varied between approximately 10 and 34 m. The sediment overburden immediately above bedrock generally consisted of well (SW) to poorly (SP) graded sands of variable thickness. The sands were overlain by low-plasticity (CL) silty clay and (ML) silt.

PREVIOUS STUDIES IN THE IMMEDIATE VICINITY

Rene and Stanonis (1995) first imaged the WIF and HLF in the immediate vicinity of our study area using deep seismic-reflection surveys. Their results showed that the WIF is composed of several branches in a quasi-planar zone, and the primary offset at depth is high-angle, north–northeast- to northeast–trending normal displacement (Fig. 4). Displacements on the lower fault branch increase with depth, whereas the displacements on the upper fault branch decrease with depth. The HLF, which lies 3 km to the east, is listric, and displacements along the fault decrease with depth. The two faults were shown to intersect within the Precambrian basement

rocks. Data based on Rene and Stanonis's study (1995) suggest the faults propagated through the late Pennsylvanian bedrock but not the Quaternary sediment (Pleistocene and Holocene). This interpretation, however, was based on poor-quality, low-resolution data from early in the time section, because the Quaternary sediment was not their primary target. The higher-resolution seismic surveys conducted in this study were specifically designed to test the near-surface sediments.

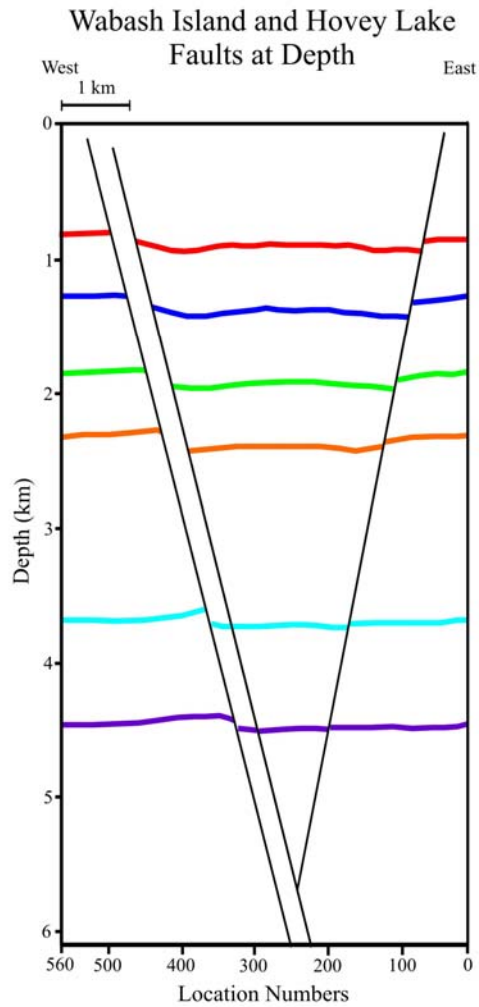

Figure 4. Structure associated with the Wabash Island fault (left) and Hovey Lake fault (right) below our elevation of interest. The reflectors shown (from shallowest to deepest) are the Ste. Genevieve Limestone, New Albany Shale, Maquoketa Group, Knox Group, Eau Claire Formation, and acoustic basement. The cross-section is displayed with 2x vertical exaggeration (modified from Rene and Stanonis, 1995).

GEOPHYSICAL METHODOLOGY

<u>SH-Wave Seismic Reflection:</u> The SH-wave is amenable for imaging neotectonic features in near-surface sediment (< 100 m) because it is a framework wave that samples the low-velocity

geologic sediment more accurately than the fluid-sensitive P-wave (i.e., not affected by the "masking" effect of groundwater). Our experience has found that although S-waves commonly have frequencies only one-half to one-third that of P-waves, the P-waves have velocities five to 10 times higher than S-waves. Consequently, we estimate that resolution can often be improved by a factor of 2 to 3 through the use of S-waves. These geophysical characteristics are significant when investigating relatively thin low-velocity media. For example, the major reflection horizons observed in many of our profiles have an average velocity range between 240 and 360 m/s, and a dominant frequency of approximately 40 Hz. This yields a temporal resolvable limit (i.e., calculated by the one-quarter wavelength criteria of Sheriff and Geldart [1989]), ranging between 1.5 m in the very near surface and 2.2 m at the top of bedrock. The detectable limits are often considerably smaller given high-quality s-wave signal (i.e., 1/10 λ to 1/20 λ) (Don Steeples, 2002, personal communication). The spatial resolution of the subject reflecting horizons is constrained between approximately two and four shotpoints, based on the radius of the first Fresnel zone.

These imaging characteristics are especially useful for accurate identification and characterization of near-surface geologic structures in the expansive river valleys of the seismically active central United States. The sequences of soft, unlithified, water-saturated sediment cover generally possess inherently weak mechanical properties that commonly fail to transform near-surface propagated faults and folds into significant or noticeable surface geomorphic features. In addition, the long recurrence intervals for large earthquakes in the Wabash Valley that are capable of creating significant geomorphic deformation features (Munson et al., 1997; Pond and Martin, 1997) can be eroded relatively quickly. Consequently, geophysical methodology, and S-wave reflection imaging in particular, is an effective initial means of near-surface geological structure location and interrogation.

Data were collected with a 48-channel Geometrics StrataVisor NX seismograph, which is a 24-bit system with an instantaneous dynamic range of 115 db. Two inline spreads of 24 Mark Products 30-Hz horizontally polarized geophones with 7.5-cm spikes were used for the

collection of seismic data. One, two-, and four-meter geophone spacings were used, depending on target resolution and depth of survey interest. The seismic data were collected at either 0.5 or 0.25 ms sampling interval. The optimal digital acquisition filter includes a 15-Hz low-cut filter with the high-cut filter out and an occasional 60-Hz notch filter when power lines were present.

The locations of the high-resolution SH-wave seismic profiles were selected using existing low-resolution P-wave profiles from the WVFS (Rene and Stanonis, 1995). Eleven profiles totaling 8 km were collected across the vicinity of the Mt. Vernon graben (Fig. 3).
The reconnaissance profiles were collected to locate the bedrock faults. Initial plans were for 4-m group intervals; however, field conditions required the interval to be changed to 2 meters for the most of the reconnaissance surveys. As an example, representative optimal-windowed field files from the beginning and end of Line 9 (i.e., across the HLF) are shown in figure 5. A subsequent, much smaller aperture profile (Line 11) was acquired to coincident to Line 9 in order to image the approximately 10 to 30 m of Quaternary sediment overburden immediately above the fault's bedrock expression. The symmetrical shots from Line 11 were used to better identify very near-surface reflectors (i.e., as early as ~60 ms two-way travel time). Although all SH-wave reflection data were collected with the 24-bit, 48-channel engineering seismograph, conservative 12 (six fold) and 6 (three fold) trace near-offset windows were used in the final reconnaissance and Quaternary survey stacks, respectively. These small optimal windows were chosen to minimize any wide-angle static and NMO frequency-distortion effects. The narrow data window (i.e., near-offset space-time window outside the ground-roll dispersion) also minimized surface-wave interference with shallow reflections (Figs. 6–7).

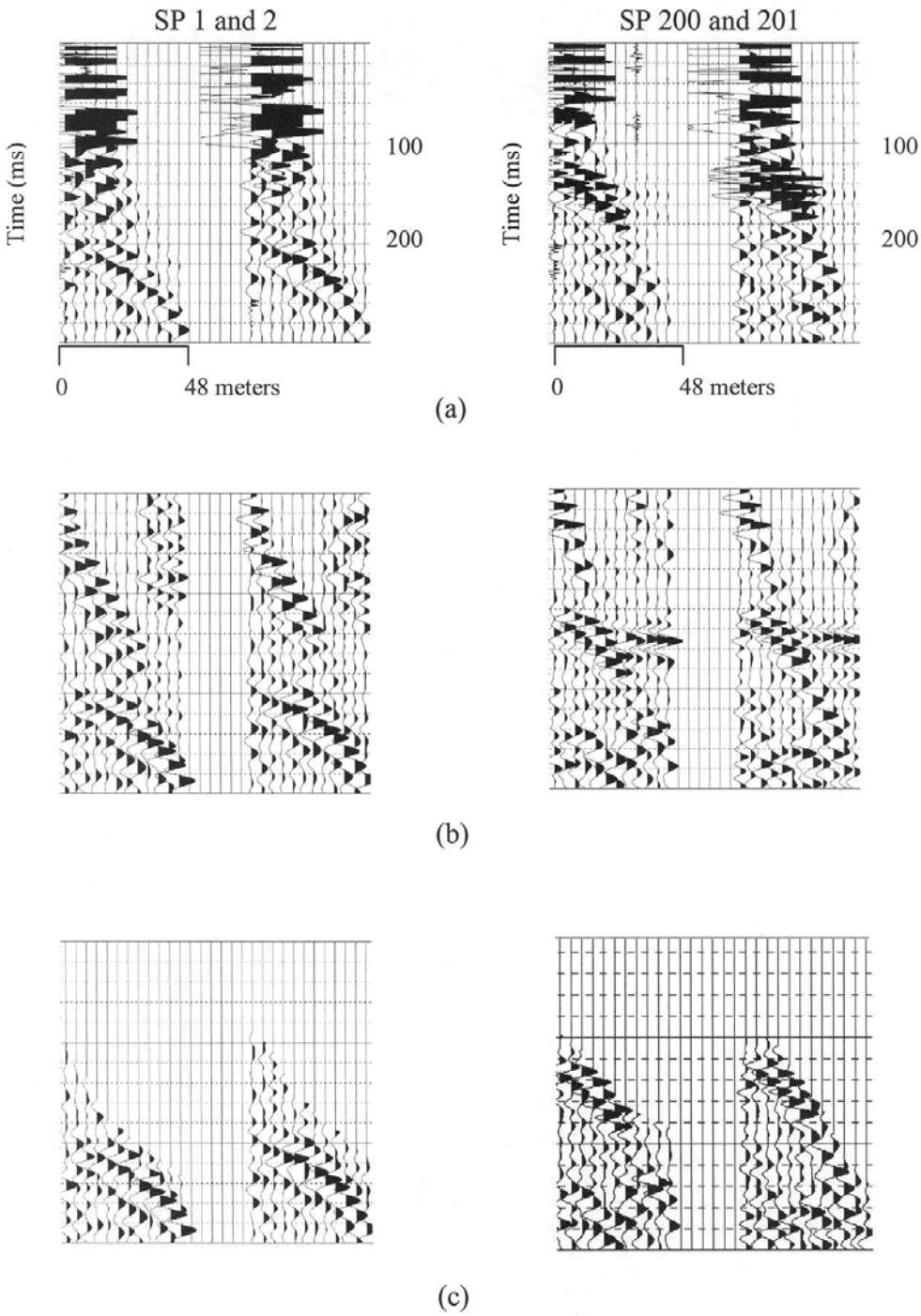

Figure 5. Representative HL-A optimal-windowed field files selected from the beginning and near the end of the survey. The data are shown as a) raw, b) bandpass filtered (30/80 Hz) with AGC (75 ms), and c) muted. A significant rise in the TWTT arrival of the bedrock reflector is exhibited over the horizontal distance of the survey. Bedrock refraction on the far traces of SP 200 and 201 is clearly visible.

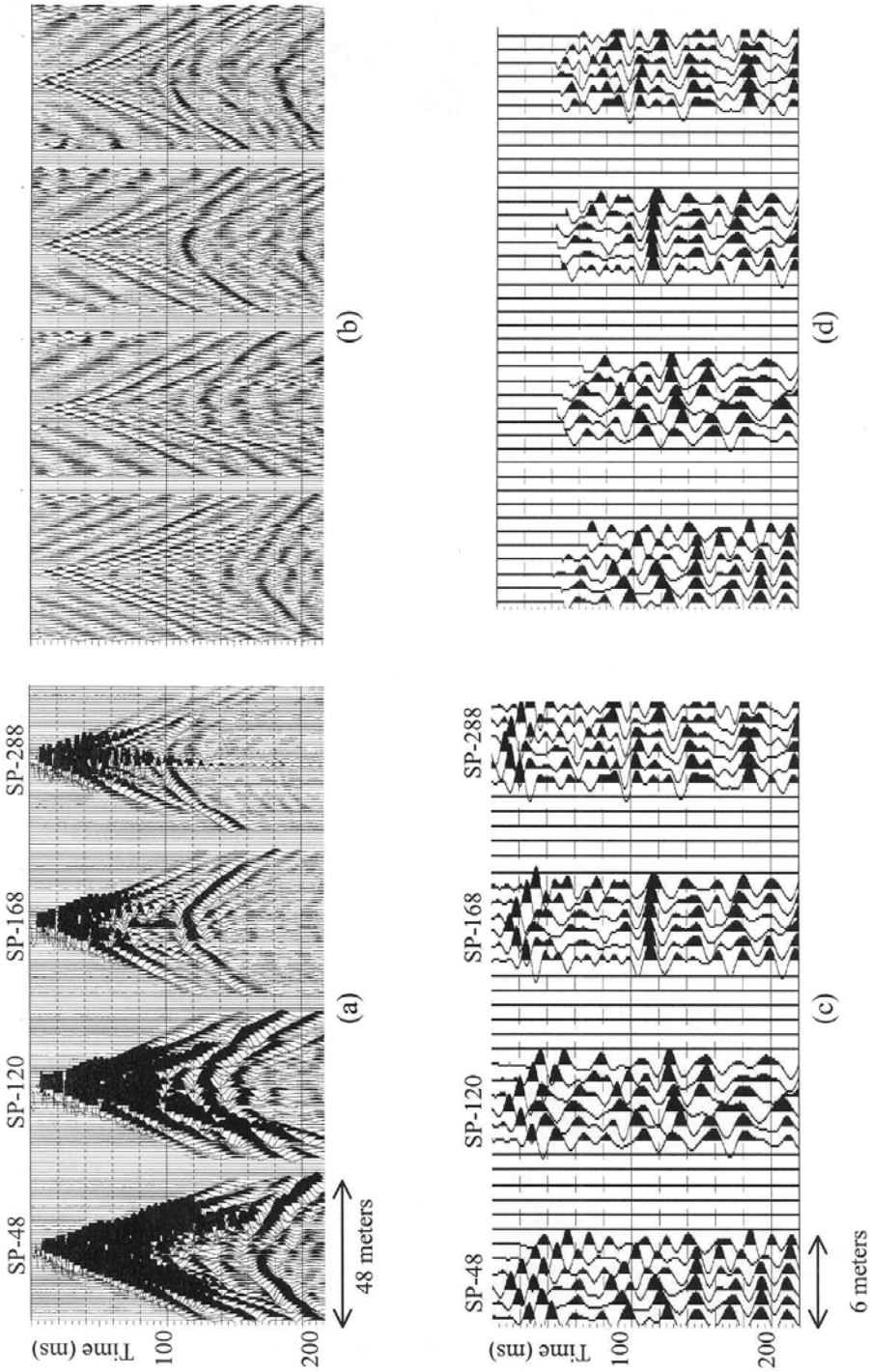

Figure 6. Representative field files were selected evenly across the Line 11 survey. The data are shown as a) raw 48-channel records, b) bandpass filtered (30/80 Hz) with AGC (50 ms), c) 6-channel optimal window, and d) muted optimal window. Progressive rise in the top of bedrock is clearly seen across the survey. Intra-alluvial reflections are discernable as high as 60 ms TWTT. Note a double hammer impact in SP-48 (c) and (d) at ~80 ms TWTT; recognition and careful surgical muting of these types of coherent noise is essential for high-quality stacks.

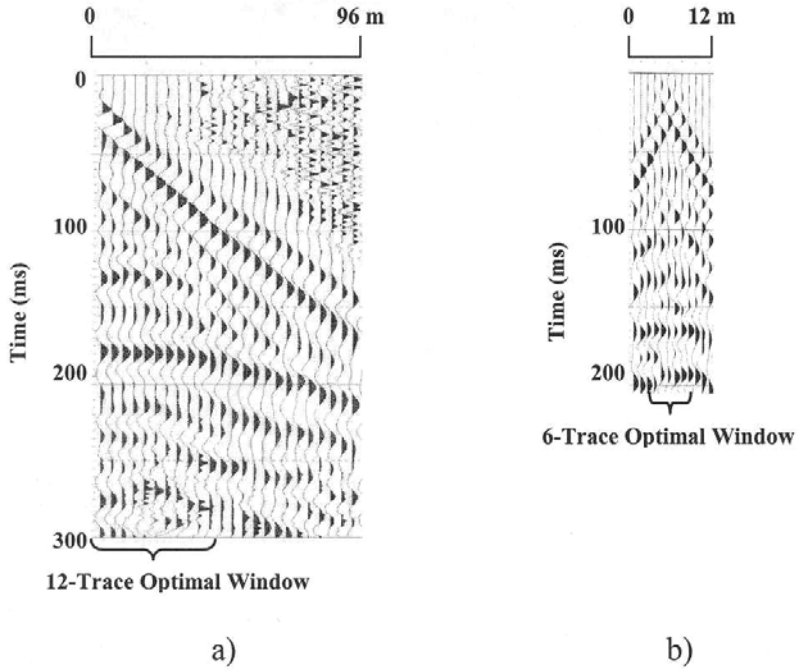

Figure 7. Selected high-quality field files from the northwest part of each survey serve as indicators for the upper range of data quality. Field files include a) 24-trace window from Line 9 SP-12 and b) 12-trace window from Line 11 SP-6. Data were viewed in various windows before the final 12- and 6-trace optimal windows for Lines 9 and 11, respectively, were selected.

The most effective energy source was a steel H-pile set in the ground and struck horizontally with a 1.4-kg hammer, as well as a 0.9 kg hammer on a 3-kg modified H-pile section for follow-up very near-surface profiling. The hold-down weight of the H-pile is 70 to 80 kg, including the weight of the hammer swinger and H-pile section. In both cases, the H-pile is set in prepared slit trenches, with its flanges struck perpendicular to the geophone spread (Fig. 8). This orientation of the H-pile relative to the geophone spread will generate SH-mode waves. The trenches provide an efficient couple between the H-pile and the earth, thus improving energy input. The most effective energy couple occurred when the H-pile was set against the edge of road asphalt. The compacted, engineered fill (i.e., higher velocity) also minimized surface wave development. The energy source was struck on both sides, and polarity reversals were used to provide accurate identification of the SH-wave energy. During production acquisition, polarity reversal was not used when data quality was good. To maximize signal-to-noise ratio, hammer blows were stacked between three and nine times per shotpoint. Table 1 contains the specific acquisition parameters for Lines 1 – 11.

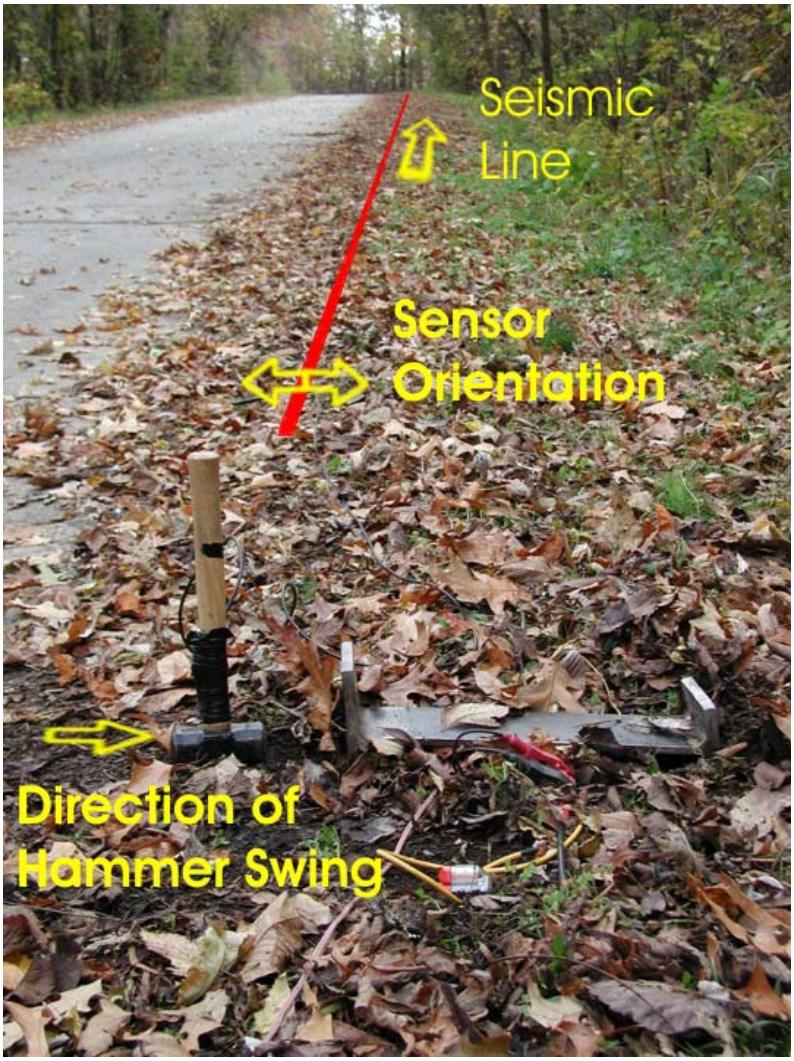

Figure 8. Relative orientations of spread, sensor, and hammer swing. Steel H-pile and horizontally polarized geophone are located bottom right.

Table of Aquisiton Parameters									
Line #	Near Offset (m)	Shot Interval (m)	Geophone Spacing (m)	Record Length (s)	Sample Interval (ms)	Acq. Filter - Low Cut (Hz)	Acq. Filter - High Cut (Hz)	60 Hz Notch Filter	Geophone (Hz)
1	0	2	2	1.024	0.5	15	Out	Yes	30 Hz
2	0	2	2	1.024	0.5	15	Out	Yes	30 Hz
3	4	4	4	1.024	0.5	15	Out	No	30 Hz
4	4	4	4	1.024	0.5	15	Out	No	30 Hz
5	4	4	4	1.024	0.5	10	Out	No	30 Hz
6	0	2	2	1.024	0.5	15	Out	Yes	30 Hz
7	0	2	2	1.024	0.5	15	Out	No	30 Hz
8	0	4	4	1.024	0.25	25	Out	Yes	30 Hz
9	0	4	4	1.024	0.5	25	Out	No	30 Hz
10	0	4	4	1.024	0.5	25	Out	No	30 Hz
11	1	1	1	1.024	0.25	10	500	No	30 Hz

Table 1. Acquisition parameters for Lines 1 through 11.

All seismic data were processed on a personal computer using commercial signal-processing software. The signal processing applied to the shallow CDP reflection data is also shown in Table 2. Coherent noise muting, digital filtering, trace editing, appropriate trace balancing, and careful correlation statics were the primary processes in improving the prestack quality of the events seen on the raw field file. This is an acceptable, routine, processing sequence for most shallow high-resolution seismic-reflection work (Steeples and Miller, 1990; Baker, 1999). These standard near-surface data-processing procedures are similar to those used in the petroleum industry, but conservatively applied. Other processing methods (i.e., deconvolution, migration, etc.) were considered but not applied, because of the lack of significant improvement in the signal quality, and the small, but inherent, resolution degradation associated with any numerical signal manipulation.

General Processing Procedures
1. Reformat
2. Spherical divergence gain
3. Bandpass filter
4. Automatic gain control
5. Elevation statics
6. Geometry and sort gathers
7. Velocity analysis
8. First-break and surgical mutes; trace kills
9. Normal moveout correction
10. Surface consistent statics (10 ms max. shift)
11. f-k filter

Table 2. Traditional signal processing procedures for the near-surface seismic reflection data.

Ground-Penetrating Radar (GPR): The GPR data were collected using the Sensors and Software Pulse EKKO 100 system in the common offset, single-fold reflection mode with an acquisition pulse voltage of 1000V. 50 MHz antennae were used and placed 2 meters apart in the perpendicular-broadside position. The station spacing was 0.5 m, and the data were collected with 32 stacks per trace in order to improve the signal-to-noise ratio. Each record length for each trace was 512 ns with a sample interval of 800 picoseconds. Signal processing of the GPR data included five primary steps: 1) signal saturation reduction, 2) time-zero adjustment, 3) Automatic Gain Control (AGC=250), 4) binomial spatial filter (3 traces), and 5) topographic corrections. The depth conversions were calculated using a constant velocity of 0.6 m/ns, which is a reasonable value calibrated by matching drilling results to GPR data observations. Coherent data were observable to a depth of approximately 4 meters, which was 1 meter less than the shallowest depth sampled by the seismic-reflection data.

SEISMIC INTERPRETATION AND RESULTS

Fault and structural interpretations were based on the high-resolution near-surface SH-wave stacked reflection profiles. Bedrock and soil layers imaged in Lines 1 through 11 are often complexly deformed. Consequently, only prominent and coherent features that are well within the resolvable limits will be interpreted on the figures and discussed in the text. Deformation above bedrock is the most important, because it reveals the nature of the most recent tectonic activity. In order to discriminate between structure and nontectonic features, anomalies had to be exhibited over multiple horizons. Orientations and location of seismic lines are displayed in Figure 3. Uninterpreted sections are shown in Appendix A.

Depth to bedrock was determined from borehole logs WI-1 and HL-1 (Appendix B). The top-of-bedrock reflector was determined from its high-amplitude signal that resulted from the high impedance contrast between the loosely compacted soil and consolidated bedrock (Fig. 9). To ensure that the suspected reflector on east–west Lines 1, 2, 6, and 8 was the soil-bedrock interface, a depth calculation was completed using the stacking velocities obtained from the semblance analysis and the Dix equations. The calculation yielded a depth of 32.3 m (106 ft), which is within 5 percent of the borehole-derived depth of 34 m (112 ft). The discrepancy is

likely due to irresolvable near-surface velocity variations, or the visual distinction between sediment and bedrock (recorded by core logger) might not correlate with the change in elastic properties (seismic reflection) due to the weathered-bedrock zone that often exists at this boundary. The soil-bedrock interface reflector was coherent across the seismic sections adjacent to the boreholes. The geophone spreads used in Line 11 (1-m spacing) were not long enough to obtain a robust sampling of the hyperbolic reflection curves for an accurate semblance velocity model. Therefore, a refraction analysis was conducted to better constrain velocities (Appendix C). The velocities obtained from refraction data were used to calculate depth to bedrock. Results showed bedrock to be at a depth of 11 m on the southeast end of Line 11 (footwall of Hovey Lake Fault) and 22 m on the northwest end (hanging wall). Bedrock was at a depth of 10.85 m in borehole HL-1 (southeast end of Line 11), which is a 1 percent difference from refraction-derived data.

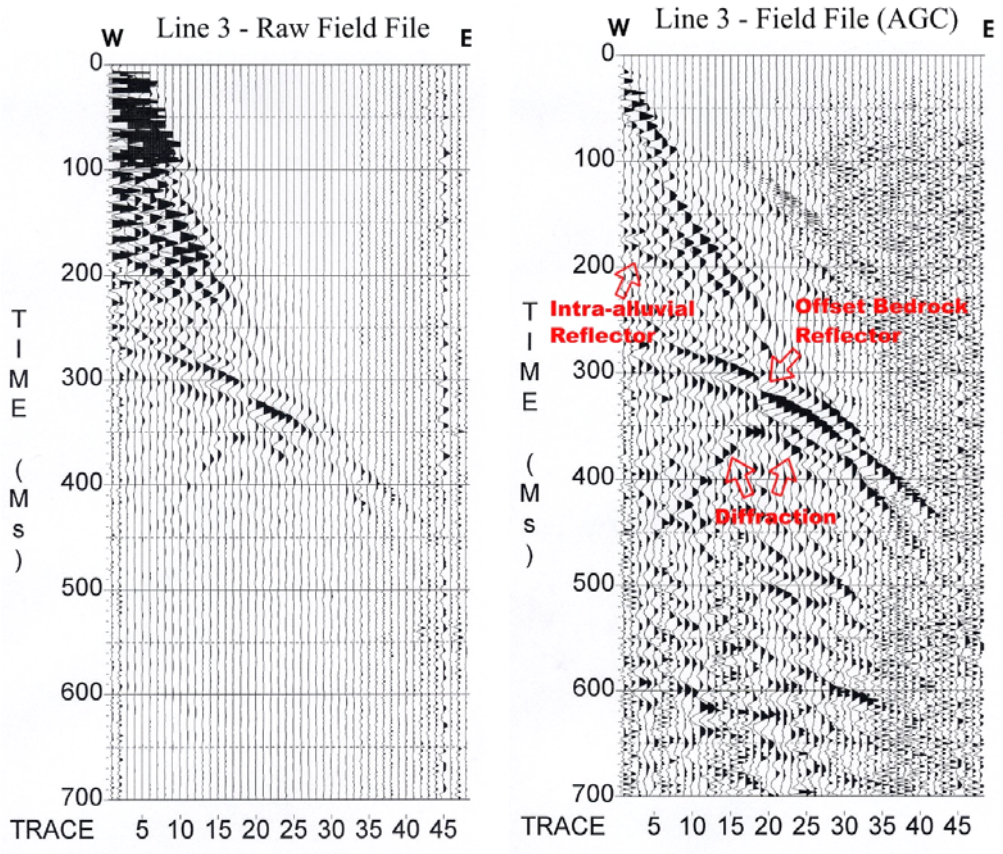

Figure 9. Raw and AGC field files from Line 3. Diffraction pattern, offset-bedrock reflector, and soil reflector are labeled in partially processed field file.

Faults were interpreted based on reflector offset, diffractions, deformation/bulging in reflectors, and loss of coherency. In general, soil reflector deformation is often not as apparent as bedrock deformation. This could be a result of the low shear strengths of the soils, the lower impedance contrast between intra-alluvial reflectors, or the soil having undergone less deformation. The low shear strength of soils means that small to moderate slip along a preexisting bedrock fault would be more likely to bend the overlying unconsolidated material than sharply offset it, especially in saturated soils.

In order to display seismic sections, vertical exaggeration is necessary. Vertical exaggeration (VE) varies with depth because of velocity fluctuations. VE's in this study will be reported for each line, but are only applicable to the soil reflectors. This is because the exaggeration changes abruptly below the soil-bedrock interface as a result of the high impedance contrast. VE's reported are based on a constant, average soil velocity from surface to bedrock. Only two VE's are reported (2.5 and 5.3) because of the similarity of soil velocities from line to line. All lines with 4-m geophone spacings will be displayed with a VE of 5.3, and lines with 1- and 2-m geophone spacings will be displayed with a VE of 2.5. An apparent consequence of vertically exaggerating a section is an increase in fault and reflector dips. Apparent fault dips reported in the text are adjusted for vertical exaggeration (Fig. 10), but not for out-of plane effects such as oblique transects across faults. Notice in Figure 10 that with a vertical exaggeration of 5.3, an exaggerated 85˚ dip translates into an unexaggerated dip of 65˚.

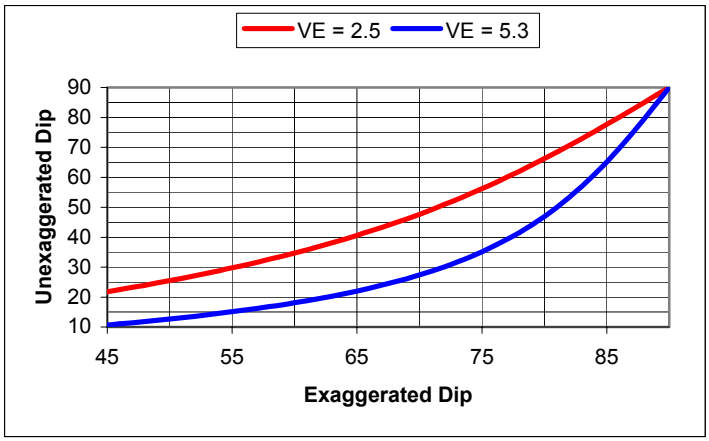

Figure 10. The relationship between unexaggerated and exaggerated dips at vertical exaggerations (VE) of 2.5 and 5.3. All stacked seismic sections with a 1- or 2-m group interval are displayed with a VE of 2.5, and stacked sections with a group interval of 4 m are displayed with a VE of 5.3.

Line 1. SH-wave seismic reflection profiles for L-1 total 1.4 km in length. Source wave input for this line was often a higher frequency than for L-3 through L-10, because the H-pile in this case was placed directly against the road asphalt. This road couple reduced movement (plastic deformation) of the plate when struck with the hammer, resulting in higher frequency and, therefore, higher-resolution data.

Interpreted profiles for L-1 are displayed in Figures 11 through 15. The average bedrock depth along L-1 is approximately 33m. The location of borehole WI-1 (CDP 571 of Figure 12) is shown on Figure 3, and the borehole description is in Appendix B.

Fault Zone 1 consists of two near-vertical faults that extend well into the Quaternary overburden (Fig. 11). The westernmost fault has an apparent dip of 88˚ to the east, and the easternmost fault has an apparent dip of 88˚ to the west. The faults were interpreted based on the loss of bedrock coherency, diffraction patterns, and bedrock offsets in the footwalls of the faults (~4.5 m of displacement across a 32 m fault zone). This loss of bedrock coherency is likely because of diffraction interference and a fractured fault zone, which makes identifying slip direction and magnitude between the faults difficult. Coherent soil reflections, however, exhibit compressional antiformal features bounded by the faults as shallow as ~18 m. The easternmost fault was extended upward to a depth of 10 m based on the series of diffractions that terminate at that depth.

Fault Zone 2 spans approximately 160 m of L-1 and contains five high-angle faults with apparent dips ranging from 78 to 85˚ (Fig. 12). Total bedrock displacement across 90 m of the fault zone (CDP 400–490) is ~6 m. Maximum bedrock displacement on a single fault is ~2.5 m (CDP 575) in a reverse motion. Soil is displaced ~2 m in a reverse motion at a depth of ~16 m (CDP 500). Bedrock is at a depth of 34 m on either side of the fault zone, but within the faulted region bedrock is uplifted to a depth of 28 m.

Fault 3 (Fig. 13) is a small-offset normal fault with an apparent dip of 73˚ extending up to a depth of 18 m. The displacement observed on Fault 3 is ~1 m, and it can be consistently

recognized from 175 to 360 ms. The combination of consistent offset in bedrock and soil layers and strong diffraction patterns was used to delineate this fault. Although the fault shows net normal displacement, bedrock layers directly on the fault bulge upward in the hanging and footwalls, implying this fault has been reactivated in a compressional sense.

Fault 4 (Fig. 14) is a high-angle discontinuity with an apparent dip of 88˚ to the east. It is similar to Fault 3 in that net displacement across the fault is minimal, strong diffractions are present up to 150 ms two-way travel time, and bedrock is uplifted ~ 1 m in the hanging and footwalls of the fault. A loss of coherency in soil and bedrock reflections further indicates deformation.

Zone 5 (Fig. 15) consists of four high-angle reverse and normal faults, with apparent dips ranging from 74 to 83˚. Reflector displacement, positive and negative folds, and strong diffractions evidence the faults. The fault farthest to the west exhibits reverse motion and the most displacement within this zone; deformation extends as shallow as ~17 m. Maximum soil displacement across this fault is ~2.5 m over a 24-m fault zone (CDP 1270–1294). Bedrock elevation across this fault is displaced ~1.5 m over a 20-m fault zone (CDP 1270–1290). The three easternmost faults all show normal displacement within the bedrock, but one fault shows reverse motion in the soil up to a depth of ~18.5 m (CDP 1305) (Fig. 15).

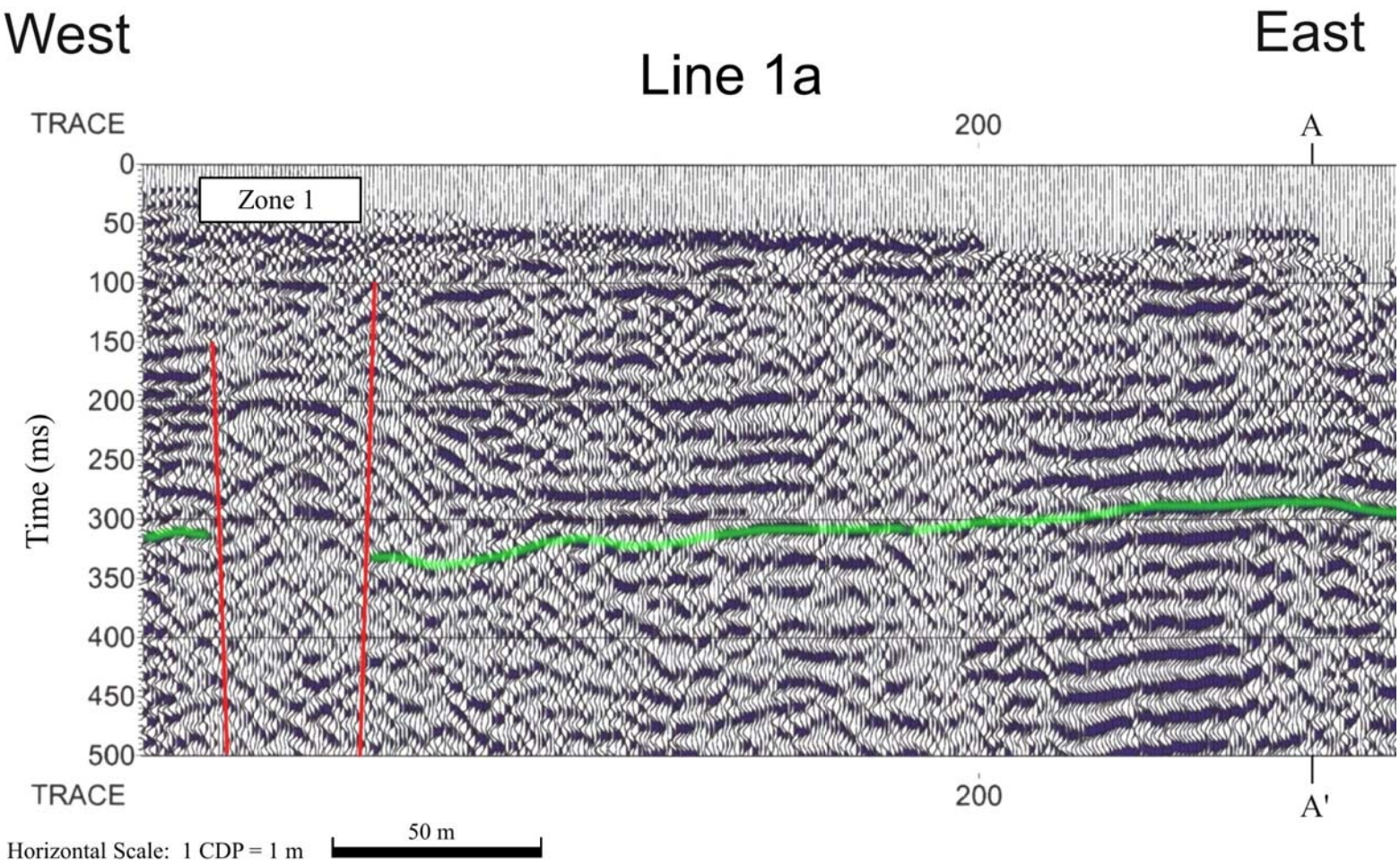

Figure 11. Section A interpretation for Line 1. Green is the soil/rock interface.

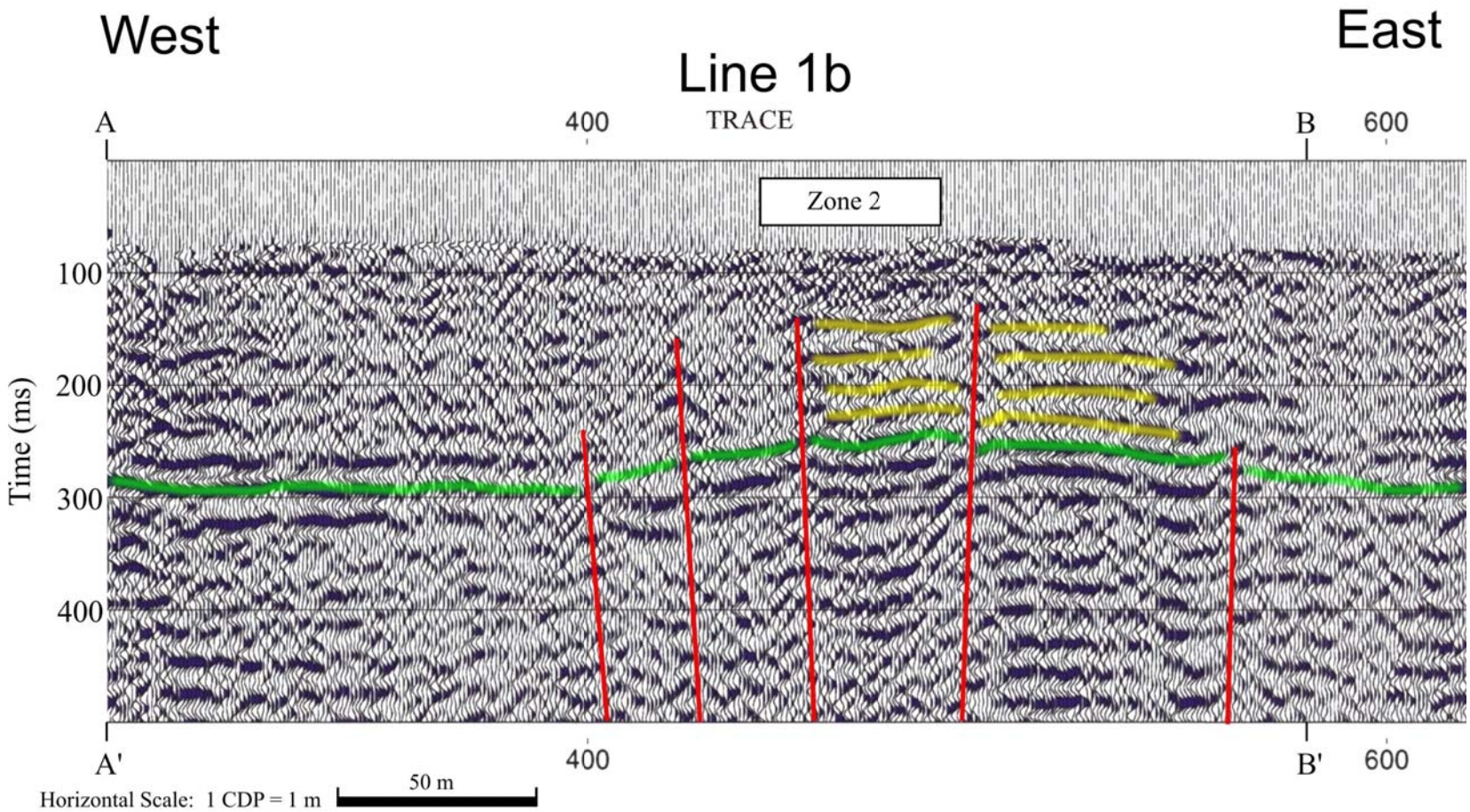

Figure 12. Section B interpretation for Line 1. Yellow represents intra-soil horizons, and Green is the soil/rock interface.

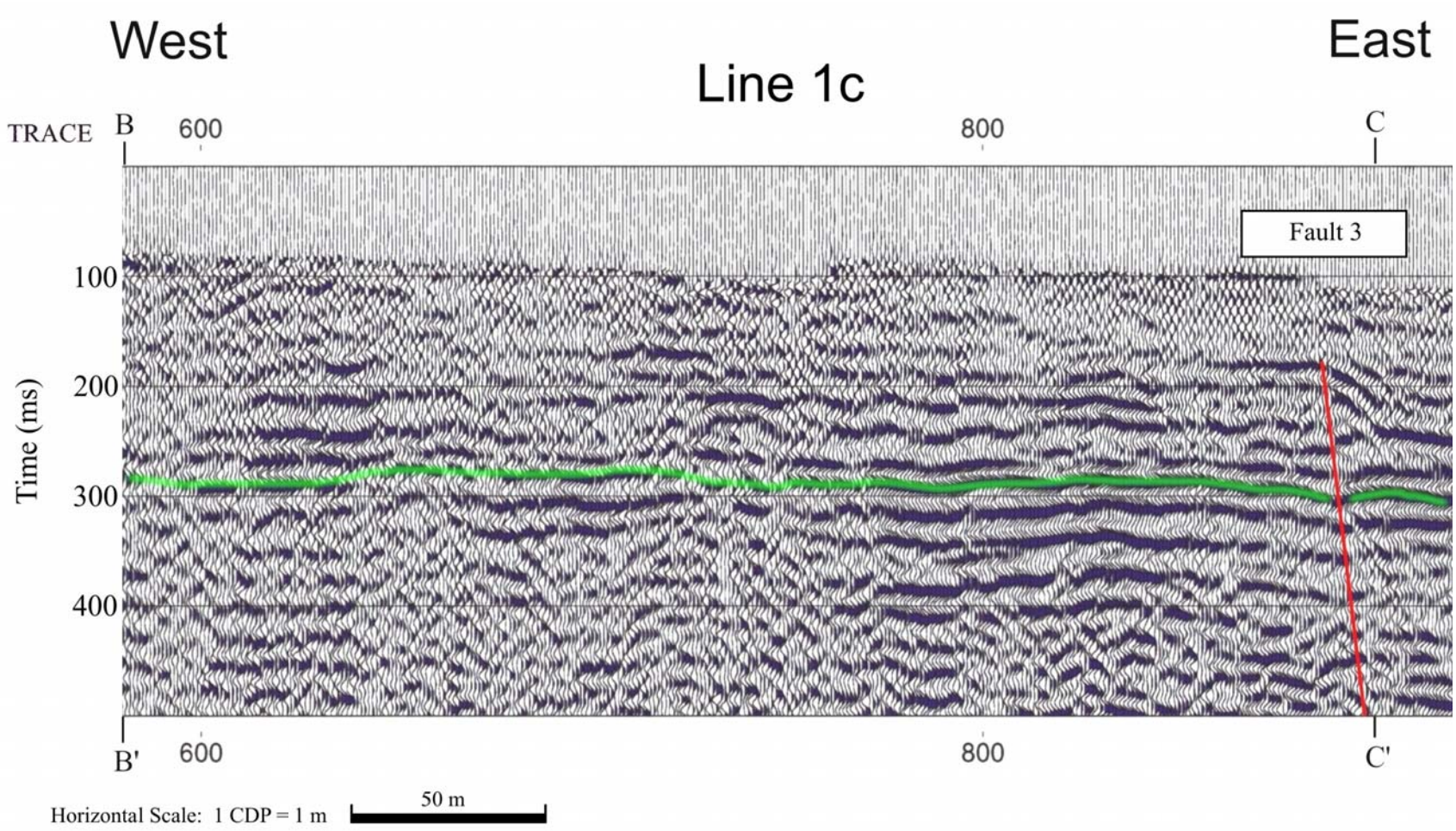

Figure 13. Section C interpretation for Line 1. Green represents the soil/rock interface.

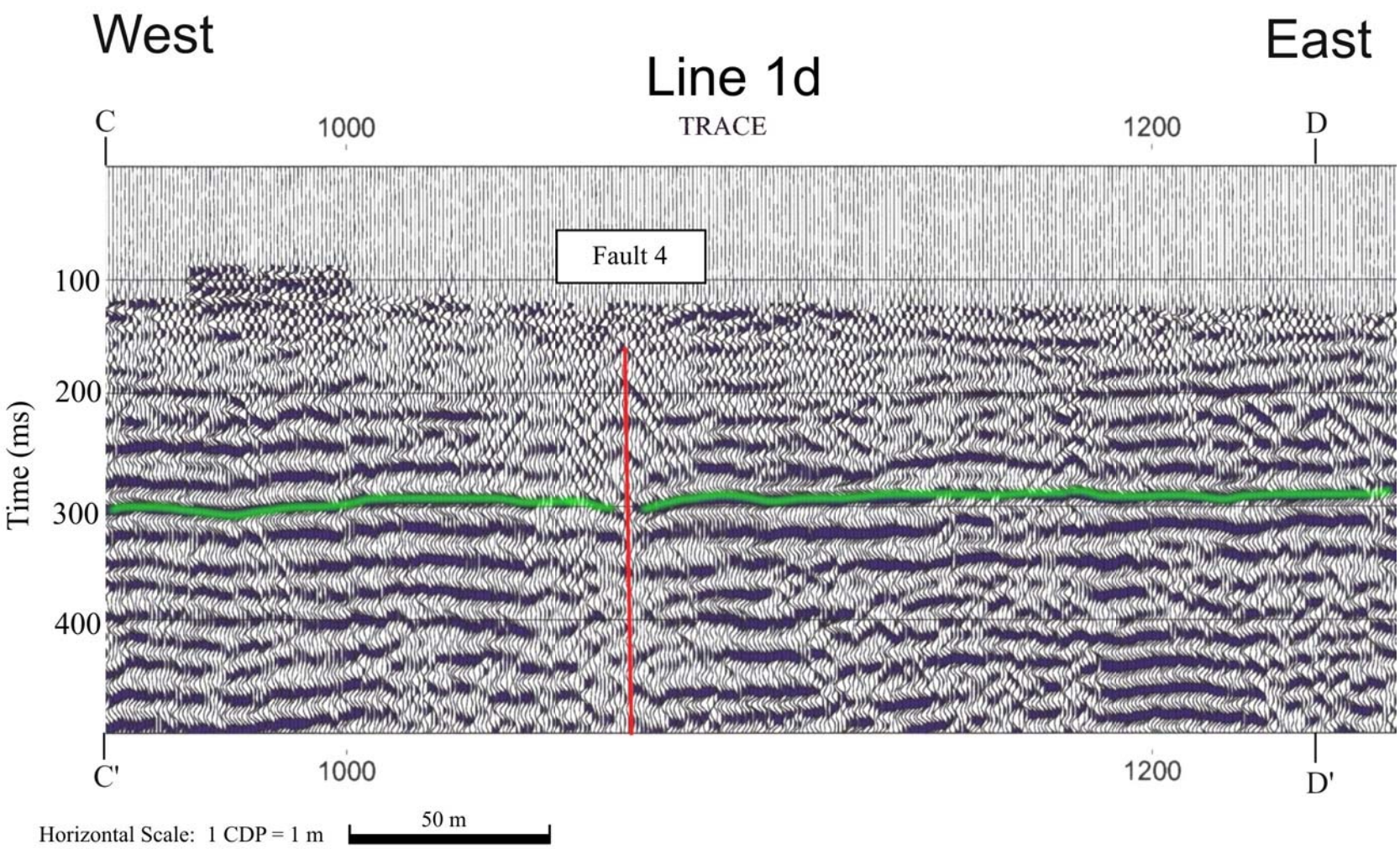

Figure 14. Section D interpretation for Line 1. Green represents the soil/rock interface.

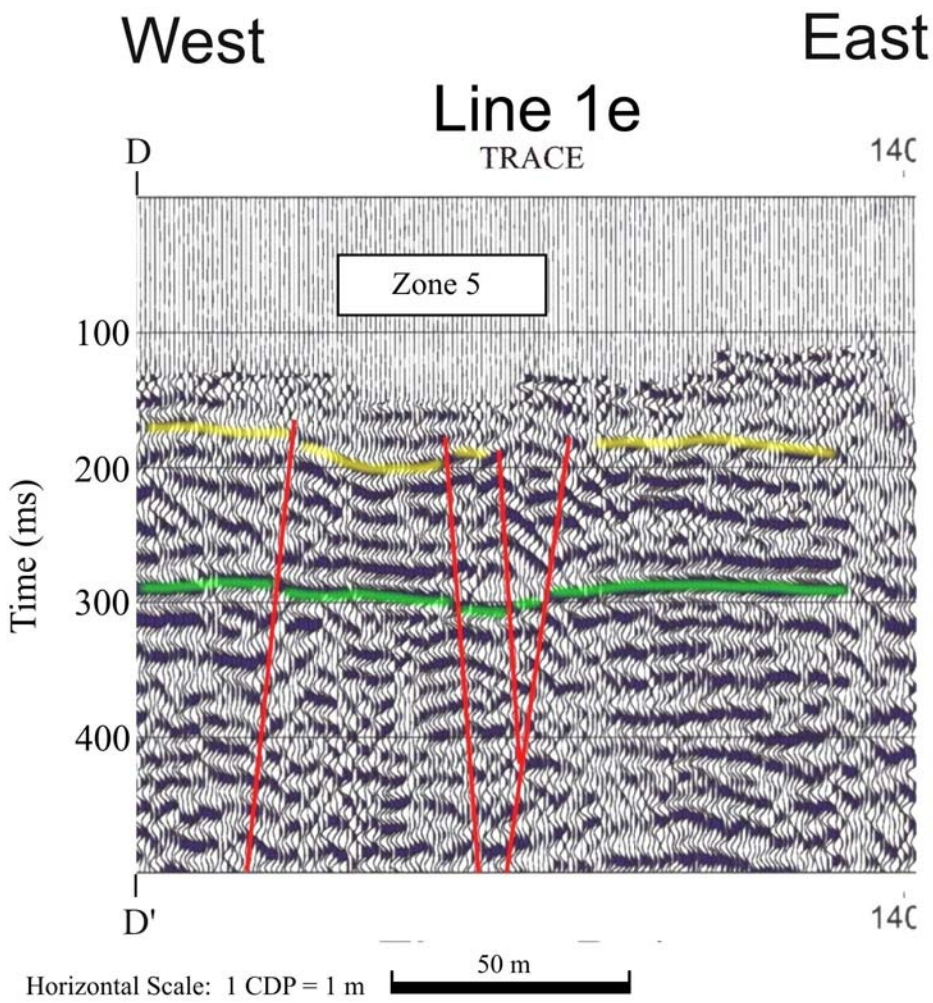

Figure 15. Section E interpretation for Line 1. Yellow represents intra-soil horizons, and Green is the soil/rock interface

Line 2. Reflection profiles of L-2 are contained in Figures 16 and 17. L-2 is an extension of L-1 that begins ~40 m east of the terminus of L-1 and continues 0.5 km east to Hovey Lake (Fig. 3). Reflection coherency and resolution in L-2 are very similar to that of L-1 because of the close proximity of the two lines, and an efficient energy couple was maintained. L-2 has an average soil frequency of 40 Hz (vertical resolution of 1.1 and horizontal resolution of 4.5 m) and an average bedrock frequency of 30 Hz (vertical resolution of 1.9 and horizontal resolution of 9.7 m).

Fault Zone 6 (Fig. 16) consists of four high-angle faults with apparent dips ranging from 71 to 83˚. The two easternmost faults merge at a depth of 45 m, and exhibit compressional strain within the branched fault zone. All bedrock displacements appear to be normally offset directly on the fault, but exhibit antiformal deformation in the footwalls and hanging walls, sometimes enough to produce net reverse motion across the fault. Maximum bedrock displacement is ~2 m across a 22-m fault zone (CDP 110–132). The soil directly above this deformed bedrock is displaced ~3 m across a 38-m zone (CDP 110–148). Fault interpretations were based on abrupt dip changes that are consistent from depths between ~10 m and ~42 m, a loss of soil coherency, and diffractions.

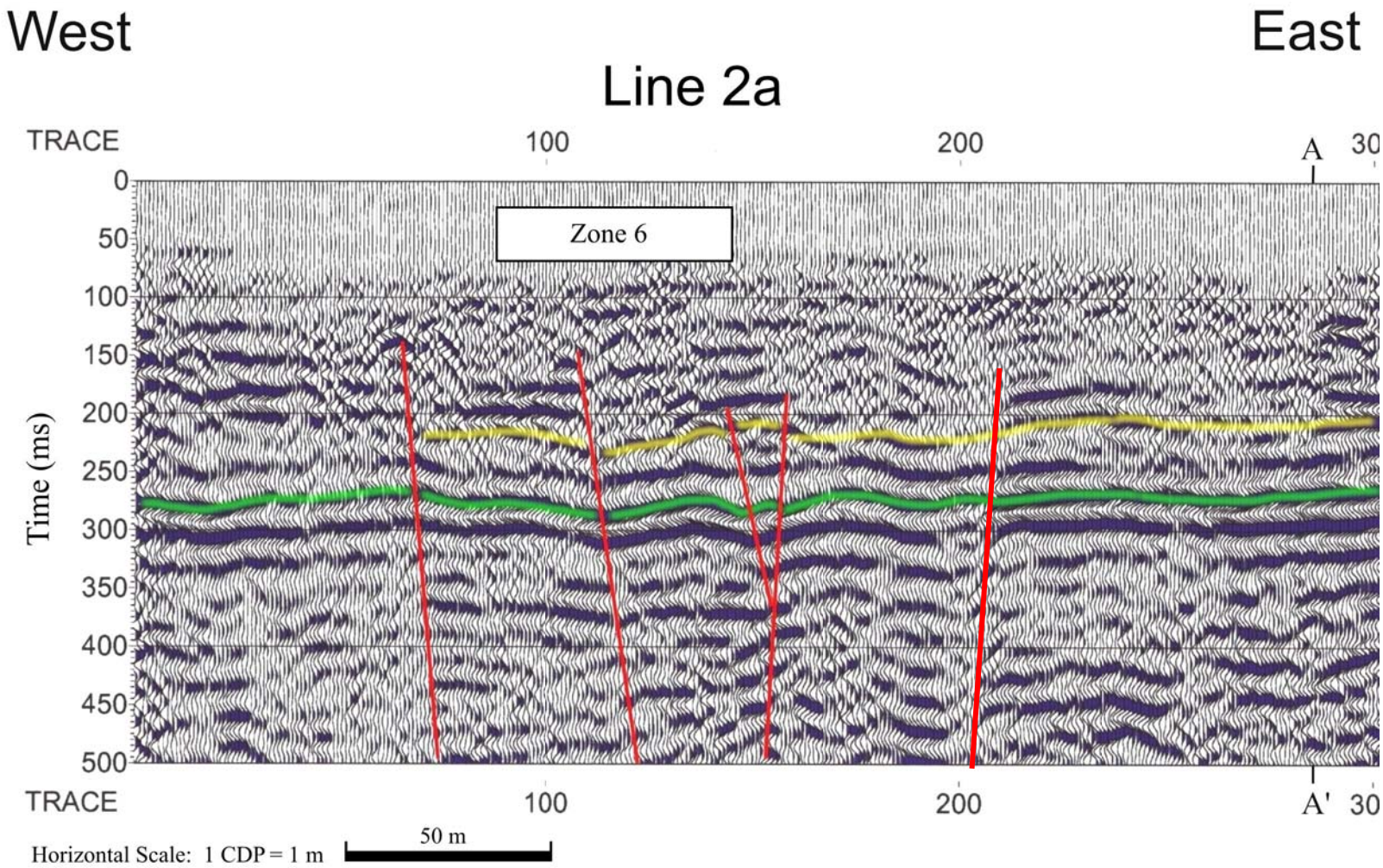

Figure 16. Section A interpretation for Line 2. Yellow represents intra-soil horizons, and Green is the soil/rock interface.

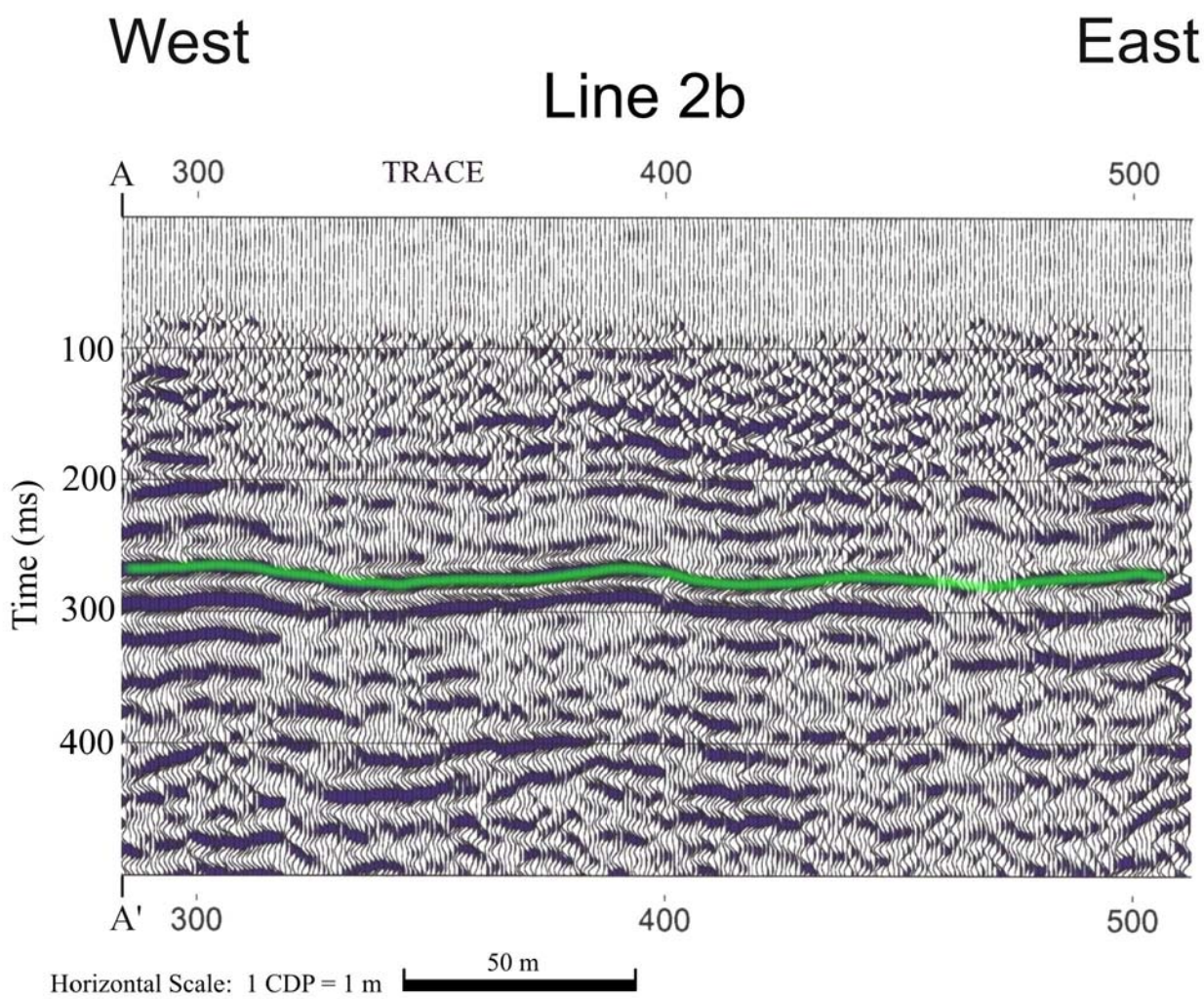

Figure 17. Section B interpretation for Line 2. Green is the soil/rock interface.

Line 3. The location of L-3 (Fig. 3), a 350-m east–west-trending survey, was chosen based on the surface projection of the HLF, as imaged by a deeper P-wave seismic reflection survey (Rene and Stanonis, 1995). HLF was targeted because it defines the eastern boundary of the Mt. Vernon graben. Data were collected on an unimproved road; the soil was not firm enough to achieve a good energy source couple relative to Lines 1 and 2. Although the profile exhibits relatively high-frequency reflections, the coherency of bedrock and soil reflections are the poorest of the 10 survey locations, possibly because of weak impedance boundaries between soil horizons, as well as poor energy coupling.

Shown at CDP 70 (Fig. 18), Fault 7 is a normal fault with an apparent dip of 70˚ to the west. The bedrock displacement on the fault as shown is ~3.5 m. This fault is interpreted to be Hovey Lake fault or a fault closely associated with it, based on several factors. First, the fault exhibits high-angle, normal displacement with the hanging wall to the west, which is consistent with the sense of motion and orientation of the previously characterized post-Pennsylvanian HLF (Rene and Stanonis, 1995). All other faults imaged in the immediate area are west of Fault 7 (see Line 4), and have the opposite sense of motion, or the magnitude of displacement is too small. Second, the location of Fault 7 is approximately 500 m east of the location at which Rene and Stanonis (1995) projected the HLF to the surface. Because of the low resolution and poor coherency of this line, the identification of slip magnitude is difficult. Consequently, this feature cannot definitively be labeled as HLF.

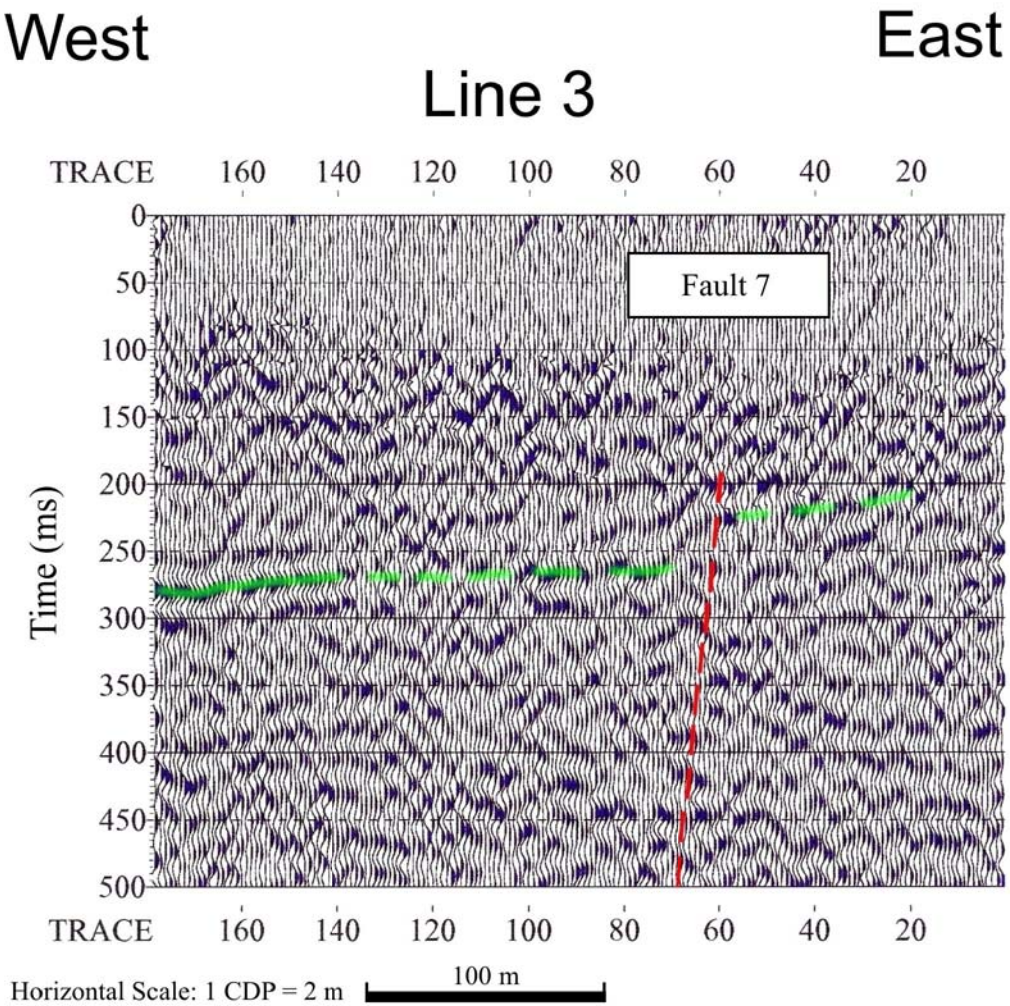

Figure 18. Interpretation for Line 3. Green is the soil/rock interface.

Line 4. L-4 (Figures 19 and 20) is the westward extension of L-3, totaling 1.05 km in length, and was collected on a stiffer road surface than for L-3. This change in surface stiffness improved the energy couple, providing better quality data than L-3. Although the data for L-4 is more coherent than for L-3, the continuity of reflections in L-4 remains poor. This may be due to extensive deformation in the soil and bedrock, and possibly weak impedance contrast between horizons. L-4 has an average soil frequency of 40 Hz (vertical resolution of 1.2 m and horizontal resolution of 4.0 m) and an average bedrock frequency of 40 Hz (vertical resolution of 1.4 m and a horizontal resolution of 8.9 m). The average bedrock depth across L-4 is ~25 m.

Zone 8 is a series of three faults (Fig. 19) with normal displacement below bedrock, and "reverse" movement in the soil horizons. The faults' dip varies at the soil-bedrock interface, from east-dipping in the bedrock (75˚ to vertical) to west-dipping in the soil (23˚ to 30˚). Bedrock displacement on the easternmost fault (CDP 310) is ~4 m over a 110-m fault zone, and the fault is upwarped in the footwall ~2.5 m between CDP 320 and CDP 375. The middle fault in Zone 8 (CDP 390) has ~2 m of bedrock displacement over a 28-m fault zone, and ~2 m of soil displacement over a 30-m fault zone. Because of a lack of coherency below the soil-bedrock interface, fault dips in the bedrock were inferred. The structural style of bedrock in L-4 suggests that bedrock is displaced normally with high-angle faults.

Zone 9 (Fig. 20) is a graben consisting of two normal faults, the eastern fault (CDP 200) having an apparent dip of 70˚ to the west and the western fault (CDP 220) having an apparent dip of 75˚ to the east. Bedrock displacement across the eastern fault is ~2.5 m, and soil displacement is ~1.5 m. The faults were identified from an abrupt change in bedrock coherency, offset bedrock and soil layers, and small diffractions.

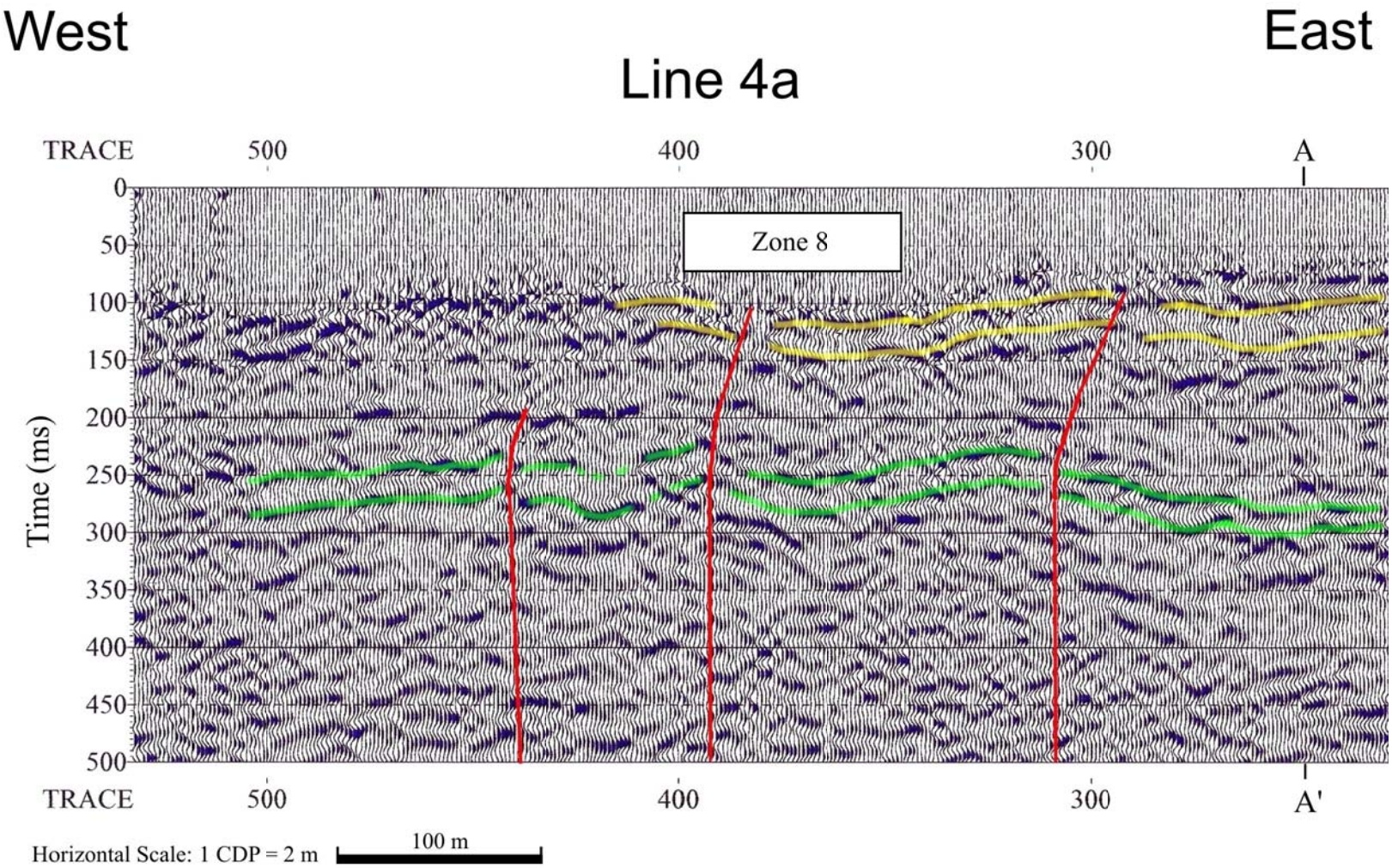

Figure 19. Section A interpretation for Line 4. Yellow represents intra-soil doublet, and Green is the soil/rock interface doublet.

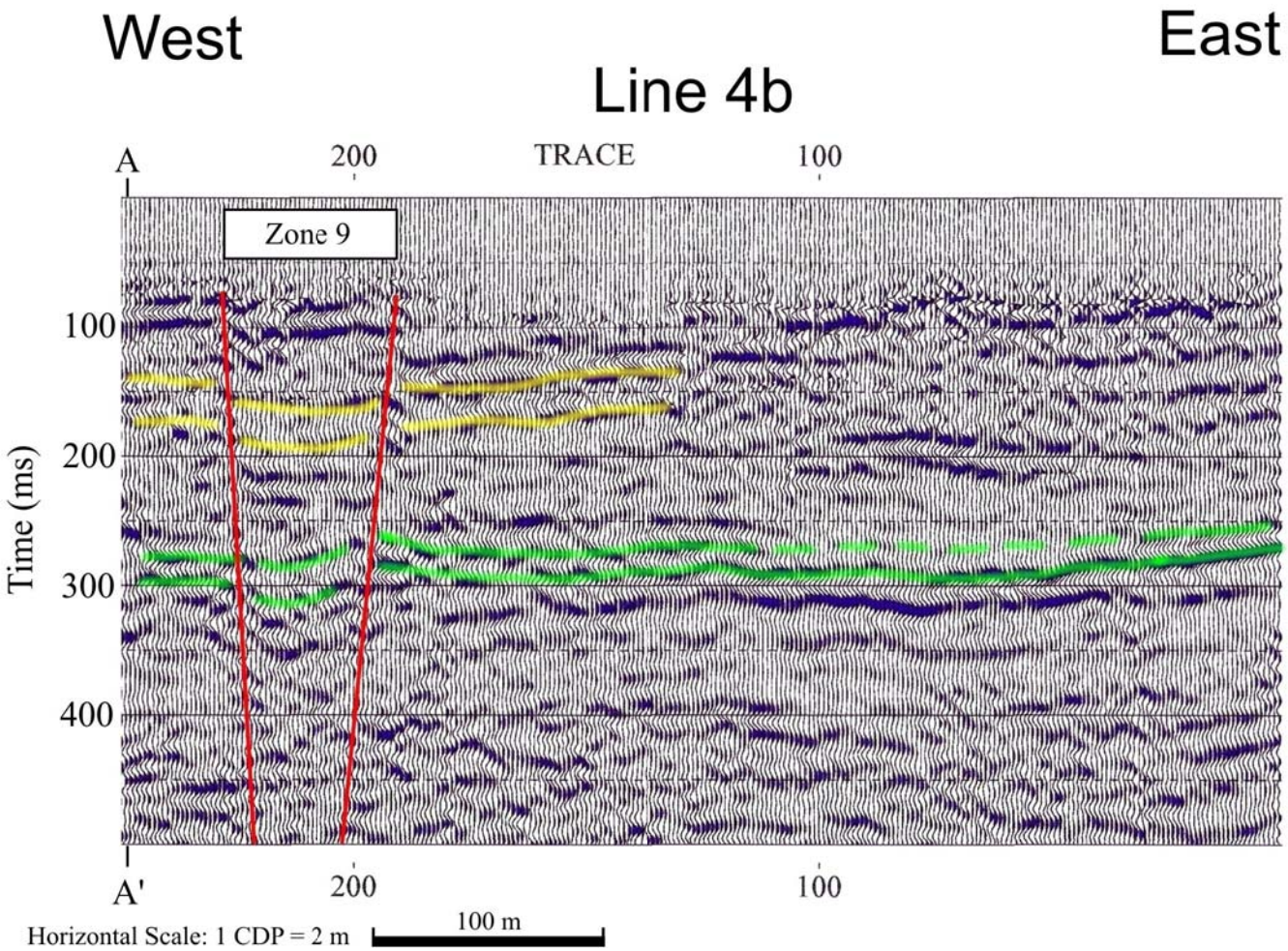

Figure 20. Section B interpretation for Line 4. Yellow represents intra-soil doublet, and Green is the soil/rock interface doublet.

Line 5. The location of L-5 (Fig. 3) was chosen based on the surface projection of the WIF, as reported by Rene and Stanonis (1995). L-5 (Fig. 21) is 620 m in length, has an average soil reflector frequency of 35 Hz (vertical resolution of 1.1 m and horizontal resolution of 4.6 m), and an average bedrock reflector frequency of 40 Hz (vertical resolution of 1.5 m and horizontal resolution of 10 m). Bedrock is at an average depth of ~30 m.

The soil-bedrock interface is coherent and variation in depth is minimal. The absence of bedrock displacement in L-5 demonstrates that the surface projection of the WIF (Rene and Stanonis, 1995) in this part of the study area is poorly defined. Soil reflectors are difficult to interpret because of low reflector coherency. No tectonic deformation can be observed in the soil or bedrock with any certainty, and therefore no interpreted faults are discussed.

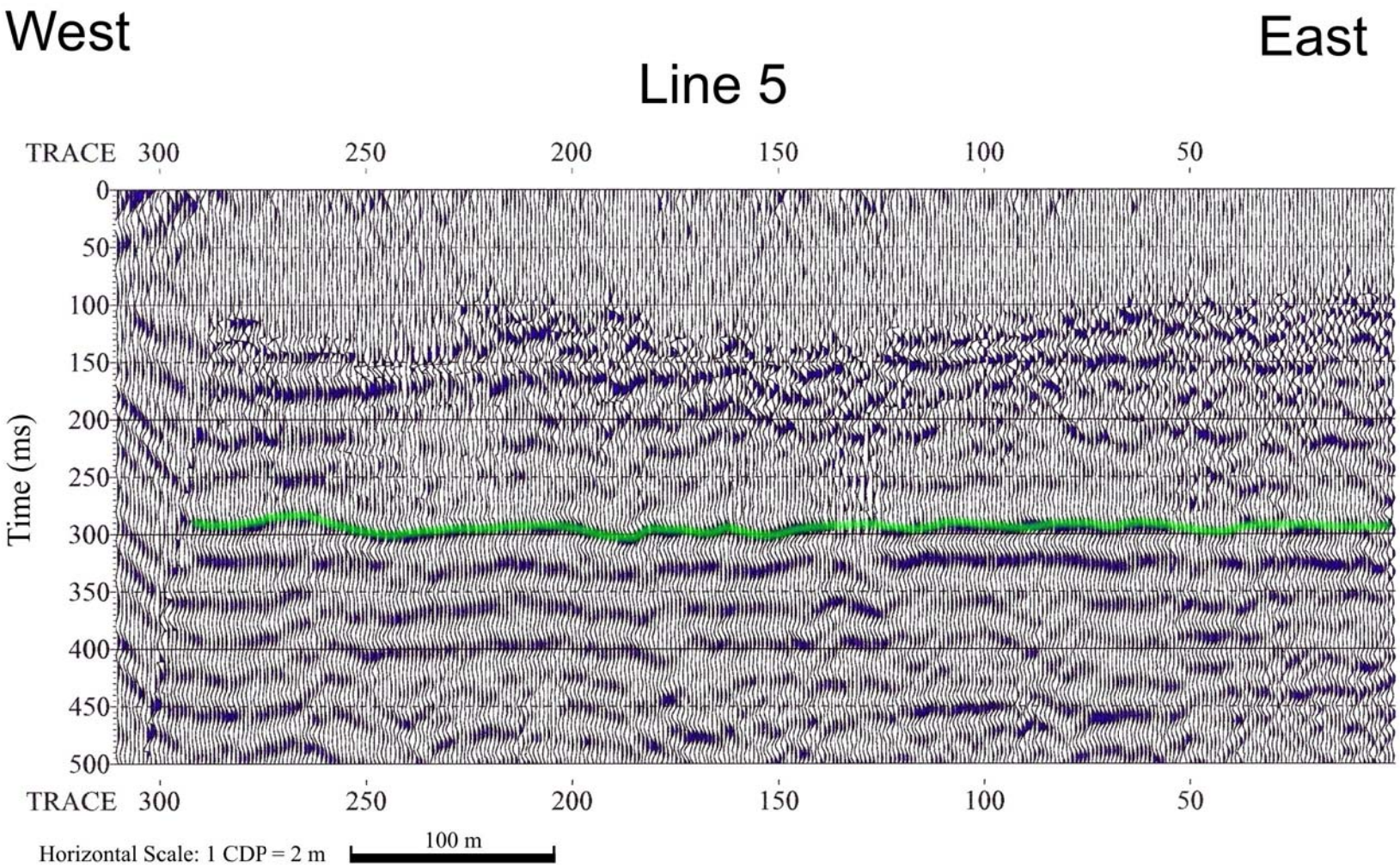

Figure 21. Interpretation for Line 5. Green is the soil/rock interface .

Line 6. L-6, located less than 30 m to the west of L-1 (Fig. 3) extends L-1 to the west and is 600 m in length. L-6 has an average soil frequency of 40 Hz (vertical resolution of 1.1 m and horizontal resolution of 4.3 m) and an average bedrock frequency of 30 Hz (vertical resolution of 1.9 m and horizontal resolution of 11.1 m). Bedrock is at an average depth of ~33 m.

Zone 10 (Fig. 22) is a series of normal and antithetic faults with apparent dips ranging from 54˚ to 80˚. There is a loss coherency in the hanging walls of the two westernmost faults of Zone 10, but bedrock is displaced ~3.5 m in the footwalls of the faults over a 25-m fault zone (CDP 105–130). Maximum soil displacement is on the western branch of the antithetic fault, and is ~1.5 m over a 20-m fault zone (CDP 170–190). In Zone 10, as in many other fault zones in the study area, some bedrock and soil reflections exhibit antiformal features in the hanging and footwalls of these normal faults, implying a compressional component to the strain. Soil is upwarped ~ 3 m from a depth of ~16.5 m to ~13.5 m between CDP 150 and 140; this exceeds the maximum soil displacement across any fault in this zone.

Zone 11 (Fig. 23) consists of three high-angle normal faults with apparent dips ranging from 78 to 85˚. All faults normally displace Quaternary overburden. Bedrock displacement (R4) across the easternmost fault (CDP 595) is ~2 m, and R1 on the same fault is normally displaced ~1.5 m. R3 on this fault shows less than 0.5 m of displacement, however. This may be a result of oblique fault slip displacing dipping soil reflectors (out-of-plane effect). R1 is also displaced ~1.5 m across a 14-m fault zone on the westernmost fault (CDP 541–555).

Although all faults and reflectors exhibit normal displacement directly on the fault, antiformal uplift of layers is apparent. All soil reflectors in the hanging wall of the westernmost fault are uplifted to a two-way travel time greater than or equal to that of the footwall (less than 25 m from the fault).

A large diffraction can be seen at CDP 615 at the end of L-6. The diffraction was not associated with any fault because it does not correlate to any offset reflection. There may be bedrock and/or soil displacement between L-6 and L-1, however.

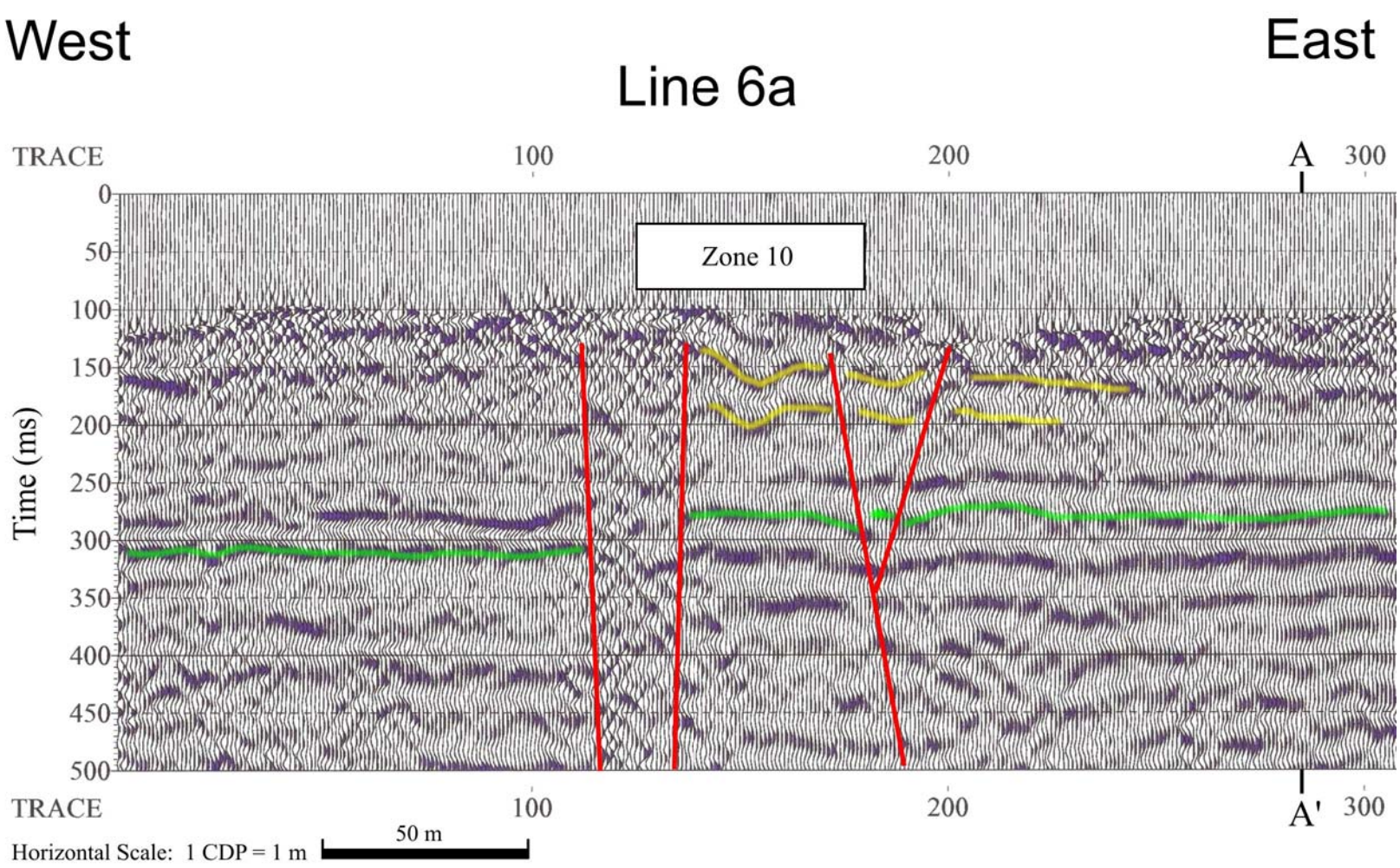

Figure 22. Section A interpretation for Line 6. Yellow is intra-soil doublet, and Green is the soil/rock interface .

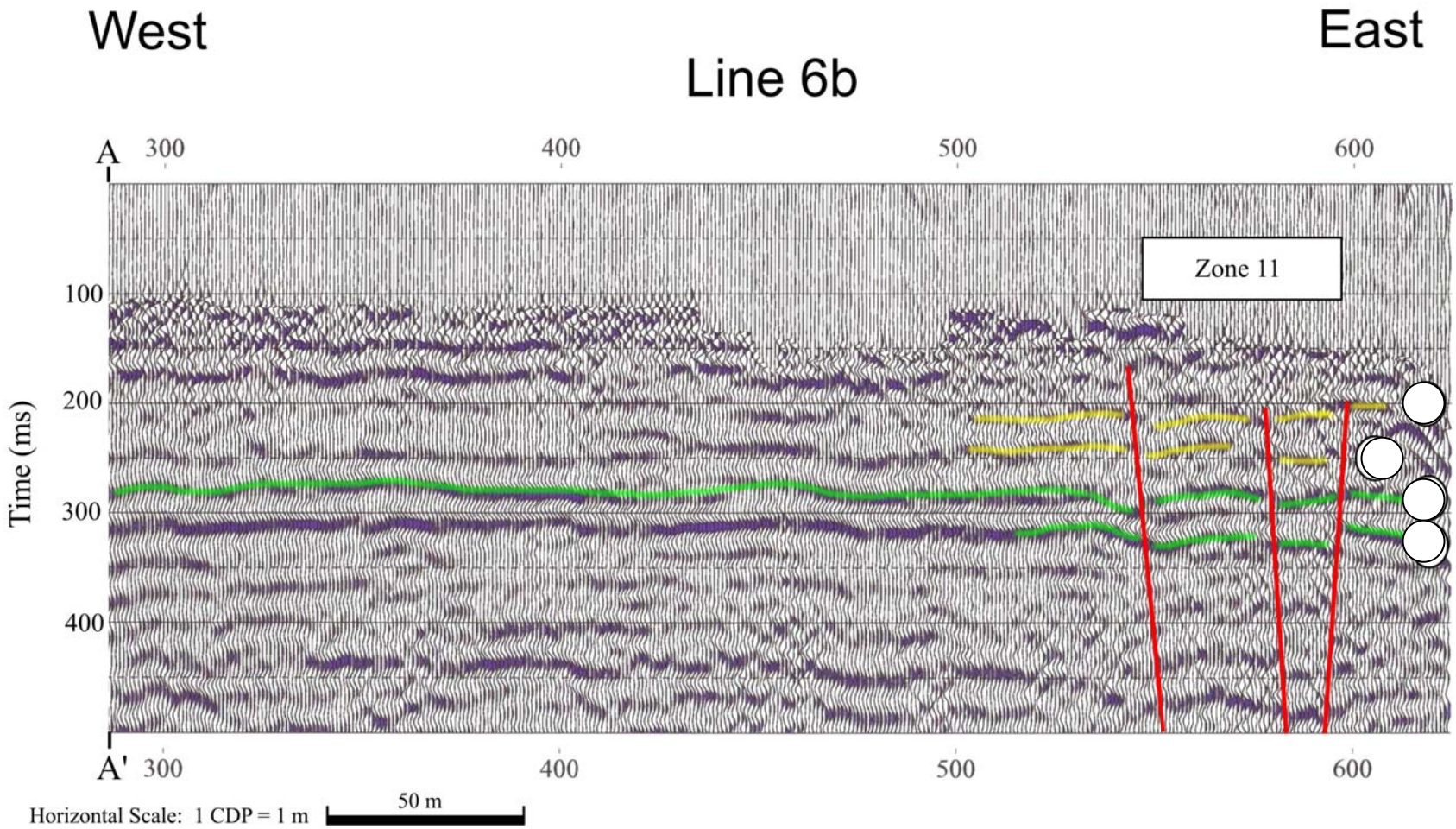

Figure 23. Section B interpretation for Line 6. Yellow is intra-soil doublet, and Green is the soil/rock interface doublet.

Line 7. L-7 (Figures 24 and 25) is a north–south-oriented line beginning near the east end of L-2 and extending 440 m to the south. This line is oriented only 20˚ from the strike of the major faults in the area, and therefore the dips, offsets, and style of faulting imaged in L-7 will be severely distorted. Although the orientation of the line was not ideal, the data was collected to complete the transect across the Mt. Vernon graben, and connect the east–west-trending lines to the west (Lines 1, 2, 6, and 8) with the northwest–southeast trending lines further to the southeast (Lines 9, 10, and 11). Soil reflectors have an average frequency of 45 Hz (vertical resolution of 1.1 m and horizontal resolution of 4.7 m) and bedrock reflectors have an average frequency of 40 Hz (vertical resolution of 1.5 m and horizontal resolution of 9.0 m). Bedrock is at an average depth of ~27 m.

Zone 12 is made up of two near-vertical faults extending to 140 ms two-way travel time (Fig. 24). Net bedrock displacement across the two faults is ~3.5 m (CDP 55–120), and both soil and bedrock exhibit monoclinal folding in the hanging wall of the southernmost fault. Net soil displacement is ~2 m across the same two faults. The combination of small offsets, bold diffraction patterns in the sediment, and abruptly changing dips at the soil-bedrock interface suggests tectonic deformation. The apparent offset across the fault zone is likely less than the true offset, because of the subparallel orientation of the profile to the regional fault strike (~20˚).

Fault 13 is located at CDP 240 of L-7 (Fig. 25). It exhibits normal displacement and has an apparent dip of 64˚ to the north. Based on previous fault-related studies (Rene and Stanonis, 1995), the orientation of the fault is more likely north-northeast–south-southwest, making the true dip greater than the apparent dip imaged in L-7. The bedrock has an apparent vertical displacement of ~2.5 m across a 32-m fault zone (CDP 245–277). Soil is normally displaced ~1 m over a 20-m fault zone (CDP 250–270). Pronounced uplift of bedrock is observed between CDP 250 and CDP 420. This results in the northern and southern ends of the line having approximately the same bedrock depth (~27.5 m), but the middle segment is uplifted to a depth of ~24.5 m.

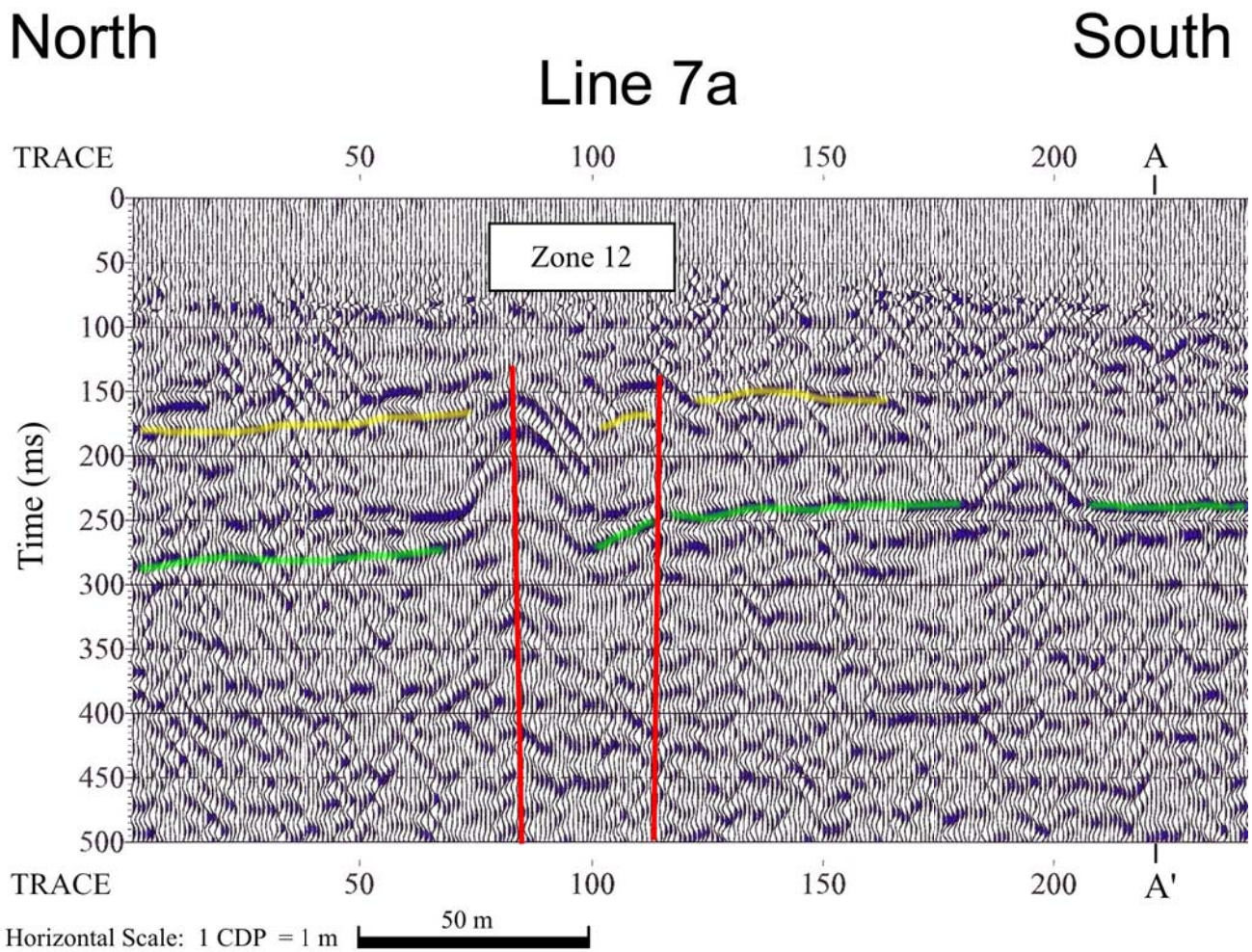

Figure 24. Section A interpretation for Line 7. Yellow is intra-soil horizon, and Green is the soil/rock interface .

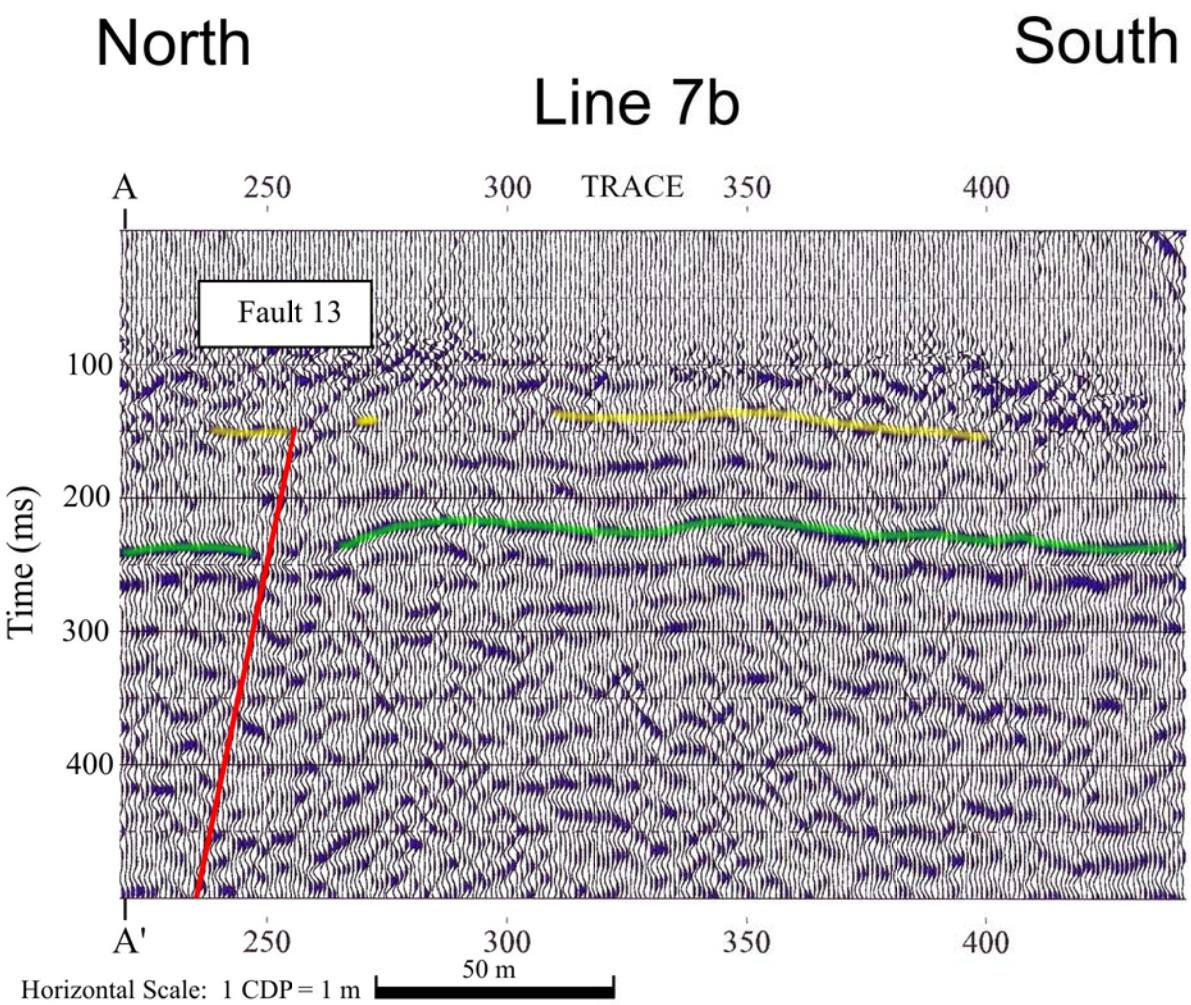

Figure 25. Section B interpretation for Line 7. Yellow is intra-soil horizon, and Green is the soil/rock interface .

Line 8. L-8 (Figures 26 and 27) is a westward extension of L-6 (Fig. 3) and is the westernmost line in the study area. L-8, 800 m in length, was collected to image the primary strand of the Wabash Island Fault (WIF) in the near surface. This location was chosen from the projection of the fault previously imaged and characterized at depth by Rene and Stanonis (1995). The average soil reflection frequency of L-8 is 50 Hz (vertical resolution of 0.8 m and horizontal resolution of 4.3 m) and the average bedrock reflection frequency is 40 Hz (vertical resolution of 1.3 m and horizontal resolution of 8.1 m). L-8 has an average bedrock depth of ~26 m.

Zone 14 (Fig. 26) consists of one normal fault and an antithetic fault with normal displacement on the rooted fault and reverse displacement on the antithetic part. The western fault dips 60˚ to the east and the primary segment of the antithetic fault dips 79˚ to the west. The western fault in Zone 14 (CDP 100) has the greatest displacement: bedrock and soil displacements are ~6 m and ~1.5 m, respectively. The western fault in this zone (CDP 100) is interpreted as the WIF. Several indicators corroborate this interpretation: (1) the fault has the same dip direction and sense of motion that the WIF has at depth, (2) the magnitude of displacement is larger than most in the area, implying it could be associated with a primary structure, (3) the location of the fault is less than 350 m from the Rene and Stanonis (1995) surface projection of the WIF, and (4) the relative density of surface faults in the vicinity of Line 8 with significant displacements is greater than that of the interpreted structures to the east, also suggesting a relation to a primary structure.

Zone 15 (Fig. 27) consists of two normal faults and one antithetic fault with apparent dips ranging from 57 to 75˚. The middle fault in Zone 15 branches at the soil-bedrock interface and exhibits reverse soil displacement on the antithetic part and normal displacement along the rooted fault in soil and bedrock. The eastern fault (CDP 225) exhibits normal displacement and dips to the west, whereas the western fault (CDP 325) is normally displaced and dips to the east. Bedrock and soil are at approximately the same depth on either side of the fault zone. Offset soil and bedrock reflectors, diffractions, and abrupt loss of coherency were primary indicators of the faults. Maximum bedrock displacement across a single fault is ~2 m over a 44-m fault zone (CDP 273–295). Maximum soil displacement is ~1.5 m over a 72-m zone (CDP 299–335), and soil is displaced in a reverse sense ~1 m at CDP 291.

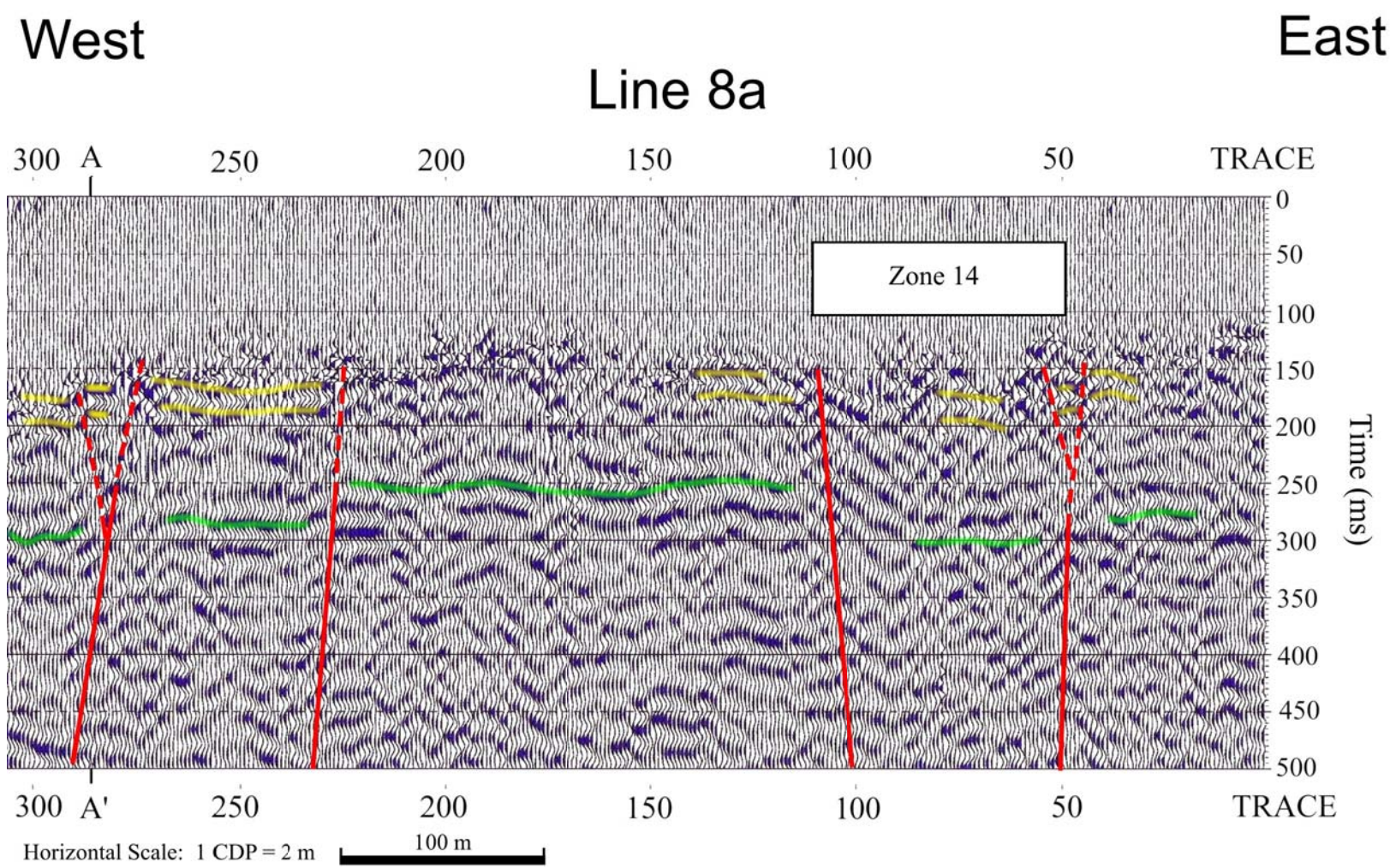

Figure 26. Section A interpretation for Line 8. Yellow is intra-soil doublet, and Green is the soil/rock interface doublet.

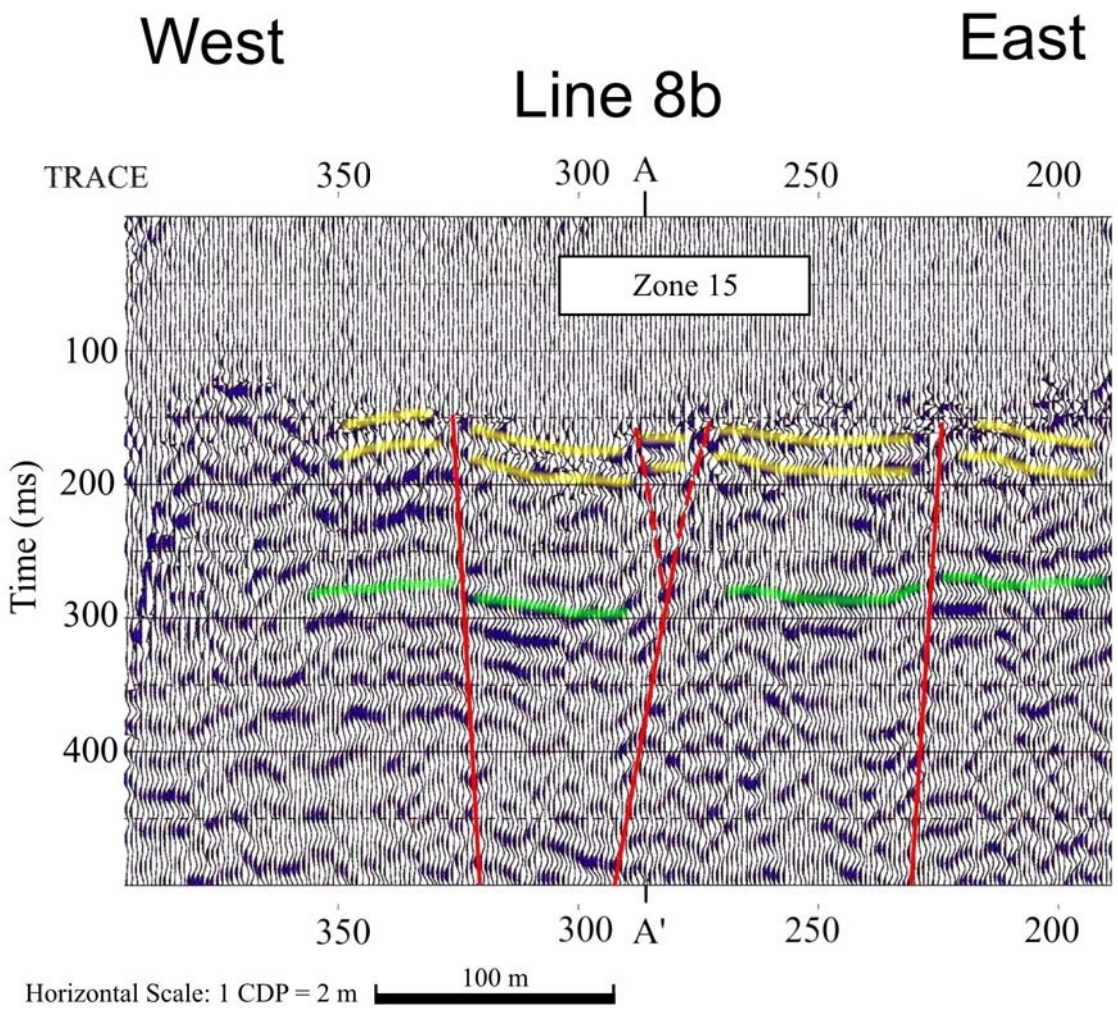

Figure 27. Section B interpretation for Line 8. Yellow is intra-soil doublet, and Green is the soil/rock interface doublet.

Line 9. L-9 (Figures 28 and 29), 880 m in length, was collected to locate and image Hovey Lake Fault, thereby completing an almost continuous set of lines across the graben formed by the Wabash Island fault and Hovey Lake fault (west to east: Lines 8, 6, 1, 2, 7, 10, and 9). The soil-bedrock interface of Hovey Lake fault was successfully imaged; however, the shallower soil reflectors (less than 10 m) could not be resolved because shot and geophone spacings were too large (i.e., 4 m), respectively, resulting in direct-wave interference within the optimum soil-reflector window. Part of this line, therefore, was reshot (Line 11) at a reduced (i.e., 1 m) shot and geophone spacing, with a 0.25 ms sampling interval and a smaller energy source (2 lb hammer and smaller aluminum plate). L-9 interpretations are displayed in Figures 28 and 29, but discussion of this fault zone will be discussed with Line 11 (section 3.5.11), where soil and bedrock deformation are observed together.

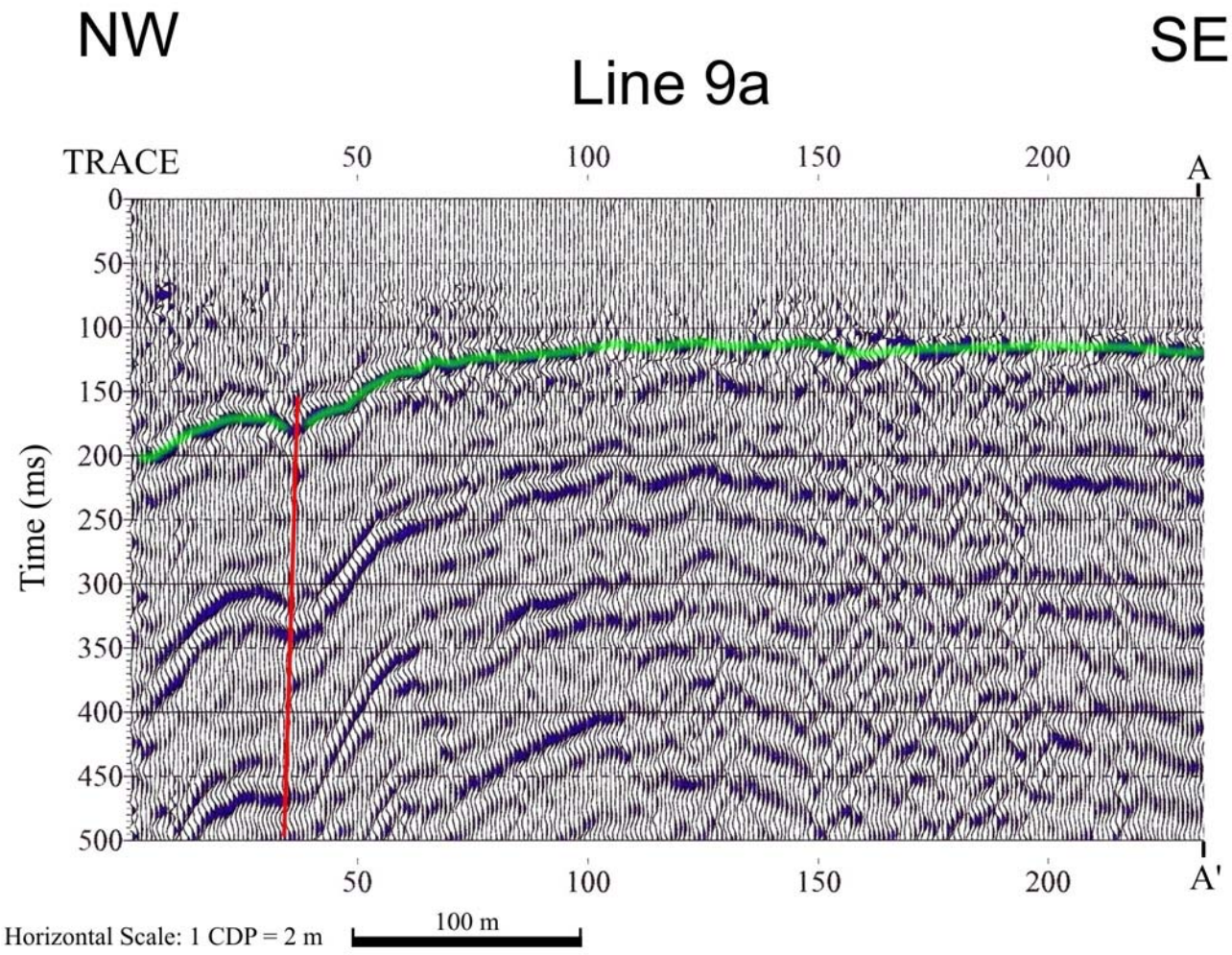

Figure 28. Section A interpretation for Line 9. Green is the soil/rock interface . Note multiples deeper in the time section.

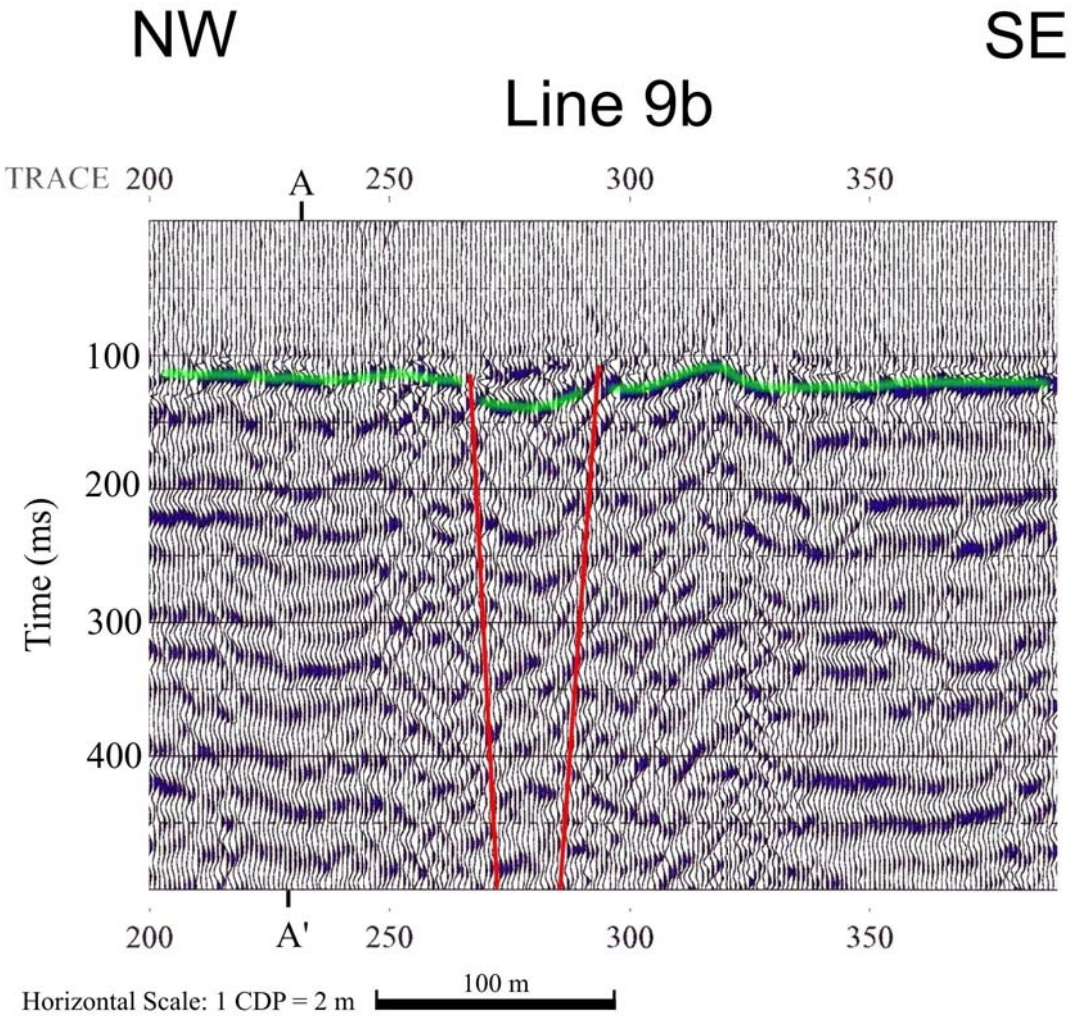

Figure 29. Section B interpretation for Line 9. Green is the soil/rock interface . Note multiples deeper in the time section.

Line 10. L-10 (Fig. 30) is an east–west-trending line starting at the first shot of L-9 and continuing westward for 215 m (Fig. 3). Soil layers were not imaged because of direct-wave interference with soil reflections. A smaller sampling interval, tighter geophone spacing, higher frequency input, and a higher low-cut acquisition frequency would likely correct this problem. Line 10 has an average bedrock reflection frequency of 50 Hz (vertical resolution of 0.5 m and horizontal resolution of 3.2 m).

Zone 16 (Fig. 30) contains two near-vertical normal faults ~28 m apart, with apparent dips ranging from 75 to 85˚. The calculated apparent dips on these faults are uncertain, because of the lack of multiple horizons (i.e., the soil-bedrock interface reflector is the only reliable reflector). The greatest displacement is on the eastern fault (CDP 35), and it is displaced ~1 m. The faults were identified by reflector displacement and diffractions.

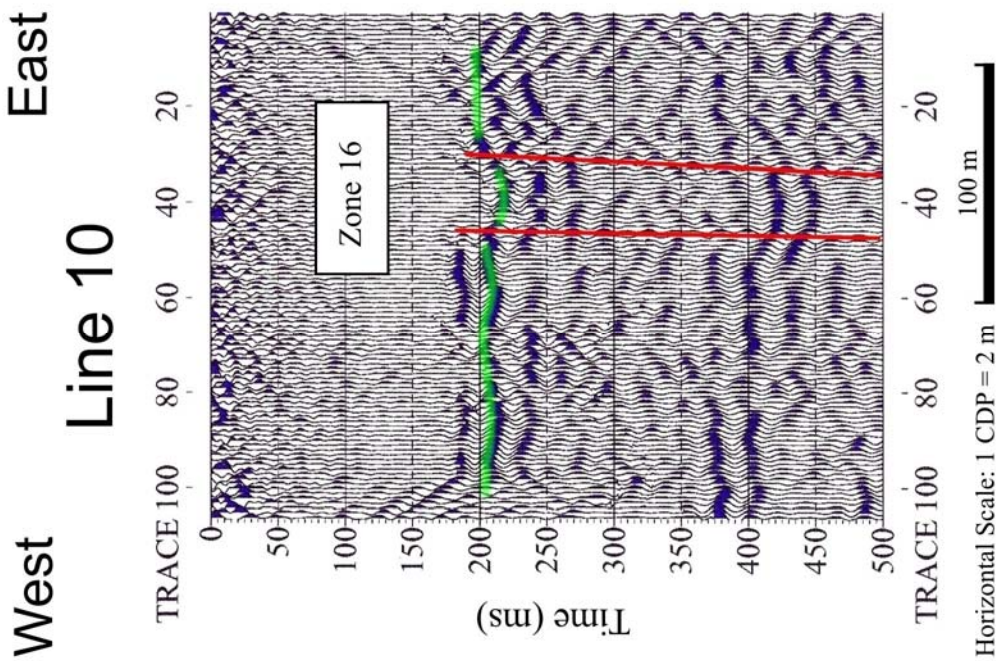

Figure 30. Interpretation for Line 9. Green is the soil/rock interface .

Line 11. L-11 (Fig. 31) is coincident with the first 290 m of L-9 (i.e., across the HLF). A reduced aperture sampled a shallower depth. Shot and geophone intervals were decreased from 4 m (L-9) to 1 m (L-11), the sampling interval was decreased from 0.5 ms to 0.25 ms, and a smaller (2 lb) rock hammer was used. Using these acquisition parameters, reflectors as shallow as 60 ms were obtained across the 300-m profile (Fig. 31), while L-9 yielded practically no reflectors above 100 ms (Figs. 28 and 29). The average soil reflector frequency of L-11 is 50 Hz (vertical resolution of 1.1 m and horizontal resolution of 5.1 m). L-11 has an average bedrock reflector frequency of 45 Hz (vertical resolution of 5.1 m and horizontal resolution of 22 m).

The HLF is seen on the bedrock reflector at approximately trace 150. The larger zone is exhibited between traces 1 and 400 as the nearly 100 ms variation (Fig. 31). Approximately 5 m of the total 10.5 m of displacement is accumulated along the bedrock horizon's steepest gradient (i.e., between traces 150 and 230). Overlying the bedrock reflector between traces 1 and 200 is as many as four relatively low-impedance intra-alluvial horizons. In this area, two relatively steep northwest-dipping reflections above bedrock unconformably underlie gentle apparent southeast-dipping reflectors at approximately 120 ms TWTT. The evidenced extension of the bedrock structure across these overlying sediment horizons is the most significant characteristic, however. The deformation affects the entire profile, including the shallowest resolvable reflector (R1) at 60 ms. R1 is calculated at approximately 5 m below ground surface, and correlates to the drilled clay-sand (CL-SP) interface (i.e., 5.7 m) found in borehole HL–1 (Fig. 32). A hinge point for a monoclinal to asymmetrical antiformal fold along R1 is defined near trace 300. An apparent northwestern dip in the reflector is evident from trace 300 to 150; the relief along this part of the horizon is approximately 3 m. There is an abrupt loss of coherency at trace 150 that is interpreted as a truncation by the primary strand of the HLF. The R1 incoherency extends laterally between traces 150 and 75; coherency is regained at trace 75, but with a 2 m inverted sense of throw (relative to bedrock throw). The southeastern side of the hinge point (trace 300) exhibits a very subtle apparent southeastern dip along R1 to trace 380. Approximately 2 m of structural relief is also noted between traces 380 and 440. Between traces 440 and 510 R1 generally appears coherent and undisturbed. R1 is again displaced 2 m down to the southeast near trace 510. The displacement is visible across all reflecting horizons on the stacked

seismogram. The remainder of the profile to the southeastern terminus appears undisturbed. The angular unconformity above the footwall, inverted offsets in the R1 deformation near trace 75, and the subtle antiformal force folds in the hanging wall, as well as the secondary small-scale deformation zones, suggest a complex structural evolution that has undergone at least one inversion from the original extensional episode. Observation of these indicators temporally through the seismic profile suggests the features are not derived from erosion or soft-sediment deformation. In addition, refraction data (Appendix C) along the line were analyzed; results show the uppermost "weathered" zone had a 1.6 m (±0.8 m) average thickness with an average velocity of 160 m/s (±16 m/s). The relatively uniform "weathered" zone, narrow near-offset acquisition window, and surface-consistent procedures minimized the potential for statics-induced artifacts.

The borehole, HL–1, drilled and sampled at the southeastern terminus of L–9 (Fig. 32) recovered two small organic deposits from the lower sand unit at depths of approximately 7.7 and 9.0 m below the ground surface. The samples were shipped to Beta Analytic Inc. for carbon-14 age determinations using the accelerator mass spectrometry method. Dates of 36,980 (±450) YBP and 39,480 (±620) YBP were derived for the 7.7 m and 9.0 m samples, respectively.

GROUND-PENETRATING-RADAR INTERPRETATION AND RESULTS

Two GPR profiles were collected (different antennae separation) coincident to the L-11 seismic-reflection survey. The clay-rich site conditions constrained the 50 MHz antennae to a maximum depth-of-penetration of approximately 4 meters (Fig. 33). This is 1 meter less than the shallowest horizons imaged by the seismic-reflection data. Reflections were identified in a limited signal window; however, two discernable displacements are interpreted. These anomalies are coincident with displacement anomalies seen at CDP 150 and 300 of the L-11 seismic survey. The numerous hyperbolic events in the deeper section are likely airwave events from a dense tree row along the eastside of the survey alignment.

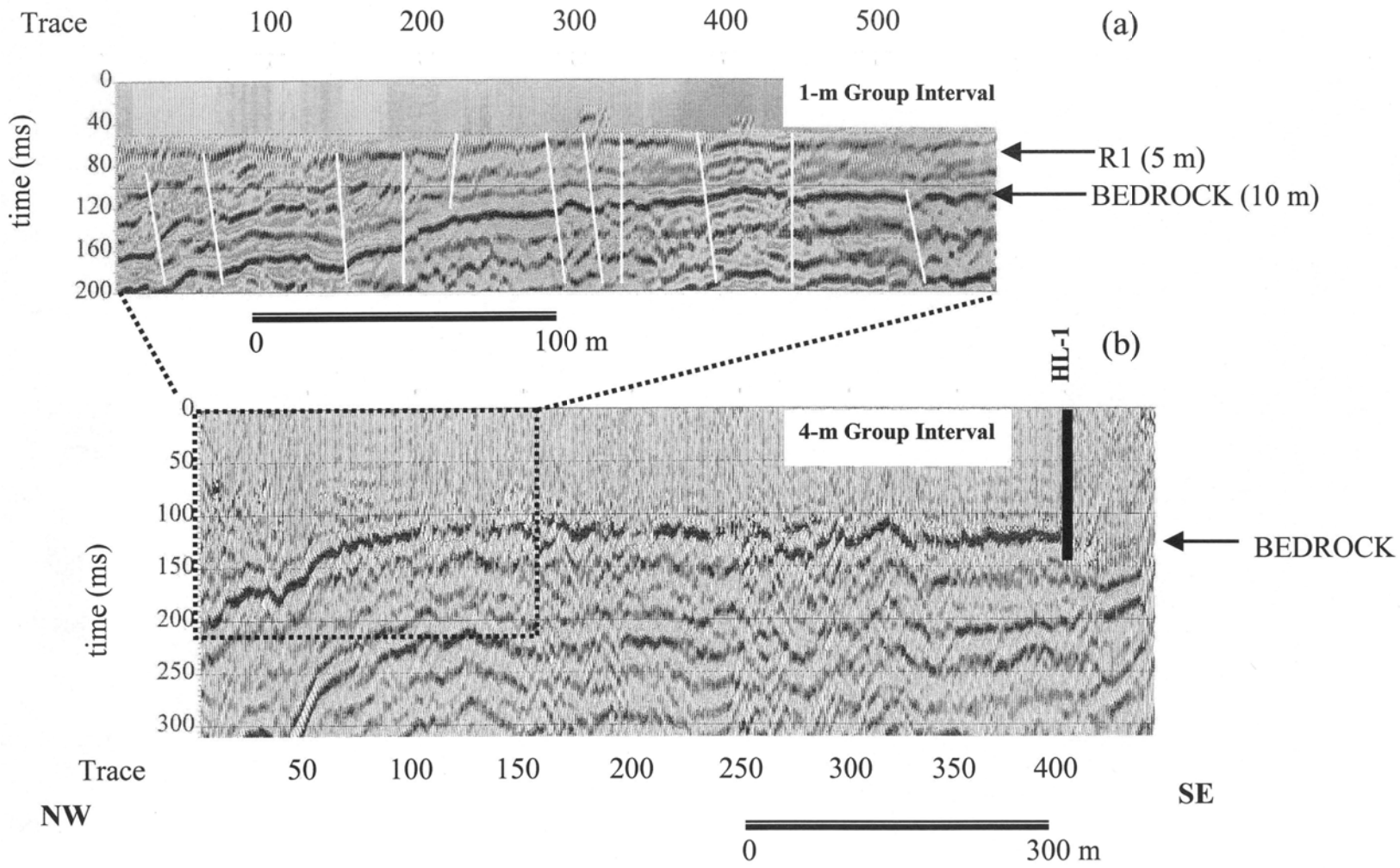

Figure 31. The stacked profiles L-9 (a) and L-11 (b) acquired across the Hovey Lake fault. The location of borehole HL-1 relative to the profiles is shown on L-9.

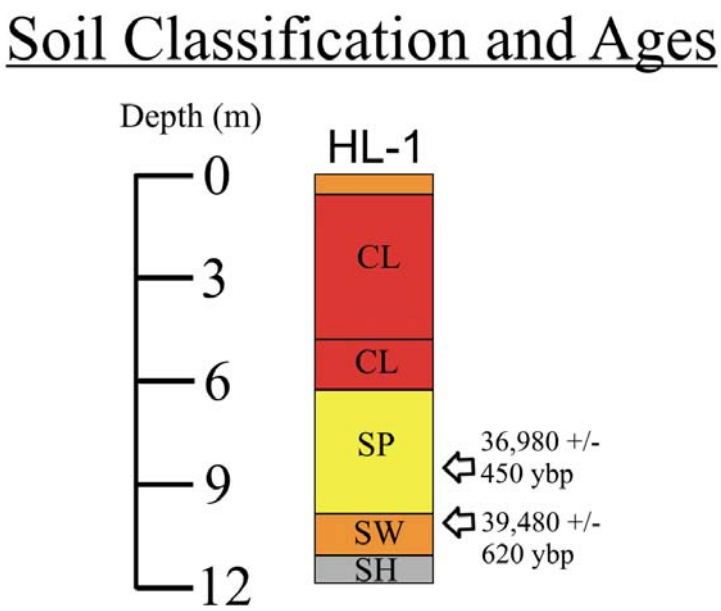

Figure 32. C^{14} dating results and soil classification from geotechnical boring HL-1. More detailed soil descriptions can be found in Appendix B.

PHASE 2 DRILLING ALONG LINE 11

Subsequent to the geophysical imaging across the HLF, an additional eleven continuously cored holes across the 300-m-wide deformation zone that was defined by the L-11 seismic profile (Fig. 33). The holes were drilled to depths ranging between 5 and 6 meters (i.e., just below the shallowest resolvable depths seen on the seismic profiles). The resultant cross-section correlates very well with the seismic interpretation (e.g., fault locations and apparent northwest-dipping fabric). More importantly, the deformation appears to extend within 2 meters of the surface. Two organic samples were recovered from the deformed horizons at 1.2 and 4.5 meters depth. The carbon-14 tests indicated that their ages were approximately 1,100 and 31,000 YBP, respectively. The latter is similar in age to the previously dated material; unfortunately the former is not well enough constrained to eliminate the possibility of post-deformation emplacement. A defensible answer will require higher-resolution analysis (i.e., paleoseismology trenching) of the structure.

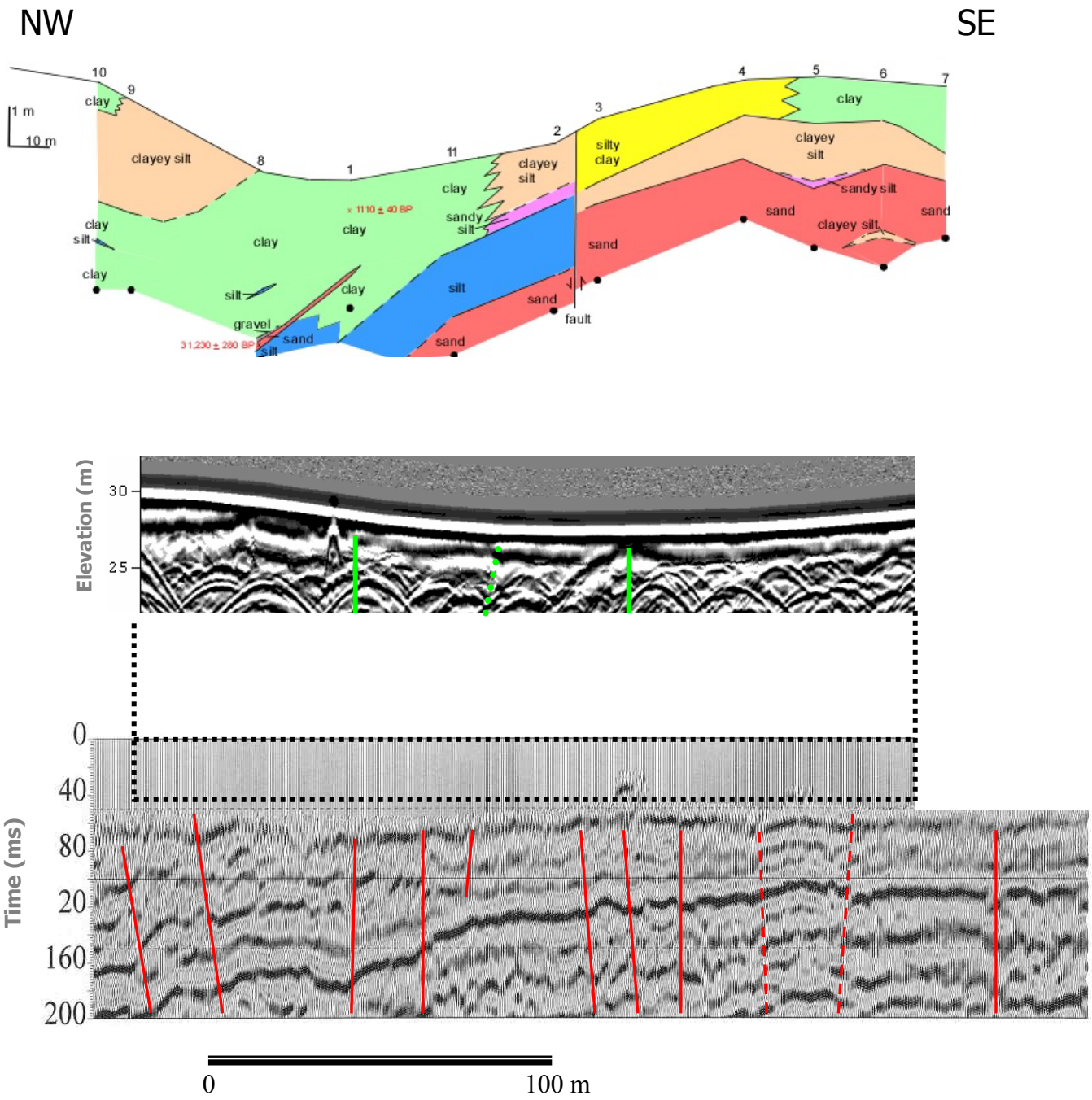

Figure 33. A GPR profile (middle) was collected coincident to the seismic-reflection survey L-11 (bottom). The depth of GPR penetration is approximately 4 meters, 1 meter less than the shallowest sampled horizon in the seismic-reflection data. The seismically opaque zone outlined by the dotted rectangle is the zone sampled by the useable GPR signal. Eleven continuously sampled soil cores (top) were subsequently collected across the seismic reflection anomalies.

DISCUSSION

The near-surface deformation observed between the HLF and WIF of southern Indiana is varied in structural style and extent throughout the study area. Forty-six discrete Quaternary faults were interpreted over the 8 km of seismic data collected. Of these faults, 23 exhibited normal displacement, 11 reverse displacement, eight were indeterminate due to loss of coherency around the fault, and four showed different senses of motion along a singe fault. Fifteen compressional features (i.e., antiformal folds or uplifts) associated with soil and bedrock faults were observed in the seismic data, and three of the 46 faults exhibited varying apparent magnitudes of slip within Quaternary sediment. The average bedrock displacement at the soil-bedrock interface (for all calculated displacements, L-1 to L-11) is ~3.4 m (ranging between 1 and 10.5 m), and the average soil displacement is ~1.7 m (ranging between 1 and 3 m). Previous work in the WVFS (Rene and Stanonis, 1995) indicated that bedrock faults imaged in this study are likely oriented north/northeast–south/southwest, and because most faults that offset soil horizons are near-surface projections of bedrock faults, their orientations are likely parallel.

The wide range of deformation types observed in the near-surface faults of the WVFS suggests a complex relationship between the regional stress field and regional crustal anomalies (i.e., ancient bedrock faults). All bedrock faults imaged in this study are high angle and interpreted to be originally formed under an extensional stress regime. The majority of soil-penetrating faults is high angle and normally displaced; however, a significant amount of compressional deformation is also observed in the form of reverse faults and antiformal folds in soil and bedrock. Normal faults, reverse faults, and uplifted sediment all within a 200-m fault zone, are not uncommon. The existence of these varied styles suggests the structures were likely acting in a predominantly transpressional manner.

Nearly all faults that offset soil horizons are near-surface projections of bedrock faults. This allows us to infer that most Quaternary deformation identified in this study is not likely the result of surficial processes (slumps, lateral spreading, collapse, etc.), and the structural style observed in the soil is partially controlled by the preexisting bedrock structure. The high-angle,

north/northeast–south/southwest-trending bedrock faults of the WVFS are currently under an east/northeast–west/southwest-oriented compressive stress (Zoback and Zoback, 1980). The diffuse seismicity throughout the WVFS indicates there are seismogenic faults within or beneath the WVFS. If the existing bedrock faults of the WVFS are being reactivated under the current regional compressive stress field, they should undergo net oblique-compressional strain. This type of strain, when acting on high-angle faults in dipping bedrock and soil, can produce a complex set of structural features that are difficult to accurately delineate in a two-dimensional survey. The sense of motion along individual fault planes imaged in two dimensions can only be resolved by knowing the site-specific fault orientation and dip, stratigraphic dip direction and magnitude, the apparent type of fault slip and magnitude (obtained from the seismic record), and the orientation of the survey line. Consequently, the description of any two-dimensional cross-sectional fault image will yield only apparent slip magnitude and direction, because of the uncertain geometric factors outside of the imaged plane. As a result of the out-of-plane effect, a series of two-dimensional surveys in an area experiencing transpressional (or transtensional) strain along high-angle faults, would likely image a wide range of apparent slip types over a relatively small area. The wide range of apparent slip types observed in the near-surface faults of the southern WVFS, and focal mechanism studies of contemporary seismicity occurring in the region, suggest that transpressional strain has been affecting the WVFS in the late Quaternary.

Focal mechanism studies of the WVFS have shown that the primary slip type associated with moderate earthquakes from 1965 to the present is right-lateral strike-slip (Taylor et al., 1989; Kim, 2003) (Fig. 34). The November 9, 1968, event (35 km west of the study area) (Fig.2), however, yielded almost pure reverse motion. Deep reflection profiles conducted by Rene and Stanonis (1995) demonstrated that the Hovey Lake fault (HLF) and Wabash Island fault (WIF) intersect within the Precambrian basement rocks at a depth of ~5.5 km, and the WIF continues into the basement rock (Fig. 4). The December 7, 2000, event (3.9 m_b), which took place approximately 5 km from the north end of HLF, occurred at a focal depth of approximately 5 km. The March 6, 2000, event (2.7 m_b), which occurred just north of Evansville, Ind., also had a focal depth of 5 km. In addition, the June 10, 1987, event, which occurred approximately 20 km north of the WVFS at a focal depth of about 10 km, had eight aftershocks, which occurred at

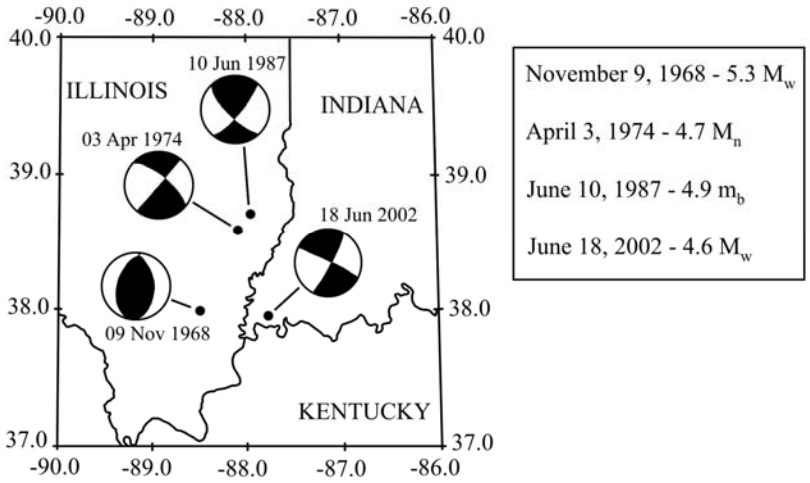

Figure 34. Focal mechanisms and locations of earthquakes in the vicinity of the Wabash Valley fault system.

depths of less than 5 km. Earthquakes occurring at depths in this range (within the boundaries of the WVFS) are likely occurring on the faults of the WVFS. In addition, small thrust faults in Mississippian and Pennsylvanian rocks with displacements of a few inches to a few feet have been identified in mines within the WVFS; many of these faults are thought to be tectonic in origin (Ault et al., 1985). These studies further substantiate the idea that the faults of the WVFS are affected by the Midcontinent Stress Province, and have been transpressionally reactivated under the east/northeast–west/southwest regional stress field.

Rene and Stanonis (1995) imaged the WIF and HLF (comprising the Mt. Vernon graben) at depth. The Mt. Vernon graben formed in extension; however, there is a broad anticline bounded by the WIF and HLF from the surface to a depth of ~4 km (Figs. 3 and 4). Rene and Stanonis (1995) interpreted this anticline to be the result of reverse-drag folding during the extensional formation of the Mt. Vernon graben. The near-surface deformation imaged in this study between the WIF and HLF, the orientation of the current regional stress field, and regional focal mechanism studies, indicate that this anticline may have formed due to, or was accentuated by, transpressional stresses after the formation of the Mt. Vernon graben.

Although evidence suggests the Midcontinent Stress Province has affected the faults of the WVFS, the Commerce geophysical lineament (CGL), which passes through the northern edge of the WVFS, could contribute to the current seismicity observed in the WVFS. Holocene fault

displacements have been observed on faults overlying the CGL (Harrison et al., 1999) suggesting a possible relationship between the basement structure and near-surface faulting events (Harrison and Schultz, 1994). In addition, at least five large prehistoric earthquakes occurred near the surface projection of the CGL (Hildenbrand and Ravat, 1997). McBride et al. (1997) showed that the hypocenter of the November 9th, 1968 event (M 5.5) (Fig. 2) coincided with basement reflectors of the CGL. The overall relationship between the CGL and WVFS remains uncertain, however.

SEISMIC HAZARD IMPLICATIONS

Carbon-14 dating conducted on organics obtained from the fifteen boreholes in the study area confirmed that soil horizons that range between 26,840 ±150 YBP and 41,040 ±740 YBP have been displaced. These dated horizons are not the shallowest imaged reflectors or the youngest 14C measurement (i.e., 1,100 YBP), but represent repeated (more confident) age measurements in the common depth range between 5 and 10 m. The shallowest imaged displaced seismic and GPR reflector is at depths of approximately 5 m and 2.5 m, respectively (Line 11). Correlative drilling over these anomalies mapped displacement within 2 meters of the ground surface. The U. S. Army Corps of Engineers and the U. S. Nuclear Regulatory Commission classify faults on which movement has occurred in the last 35,000 years as "capable." Consequently, the results in have design implications for critical structures in the region.

Obermeier (1998) described paleoliquefaction features found in and around the WVFS with calculated magnitudes of M~7.5 and M~7.1, occurring 6100 ±100 YBP and 12,000 ±100 YBP respectively. Other Holocene paleoliquefaction features have been identified in the region (Munson et al., 1997; Pond and Martin, 1997), which represent significant seismic events. The combination of late Quaternary imaged faults, paleoseismicity, and contemporary seismicity in the WVFS suggests that the southern WVFS is a source zone for more detailed seismic hazard evaluation. The techniques used in this study do not have the resolution required to characterize many important parameters (e.g., strain/slip rates or the minimum depth and age of displacement/deformation) used in a detailed assessment. Therefore, further higher resolution studies are required to define magnitude and recurrence estimates.

CONCLUSIONS

Eight kilometers of SH-wave seismic-reflection profiles, one kilometer of GPR imaging, and fifteen correlative boreholes collected in the southern WVFS suggest first-order neotectonic deformation in the Quaternary sediments overlying the reactivated Paleozoic structure. Forty-four of the 46 faults that offset or deform soil horizons are extensions of high-angle bedrock faults, supporting the hypothesis for a tectonic origin and not a result of surficial processes that can produce similar features (e.g., slumps, lateral spreading, collapse features, facies change, etc.). The average bedrock displacement at the soil-bedrock interface is approximately 3.4 m (range of 1 to 10.5 m), and the average soil displacement is approximately1.7 m (range of 1 to 3 m). Several styles of deformation in the Quaternary overburden were interpreted: (1) apparent extension, (2) compressional features, such as antiformal folding of soil layers in the hanging and footwalls of faults and apparent reverse motion along faults, (3) opposing senses of motion with individual faults, and (4) varying slip magnitude within individual faults. Varying types of slip and magnitude of slip along single faults may suggest an oblique component to the fault motion that produces an out-of-plane effect distorting the true slip direction and magnitude in a two-dimensional survey. A dipping layer or layers with varying thicknesses that are offset obliquely (or laterally) produce a false sense of motion in two dimensions.

The seismic profiles also exhibit soil and bedrock layers folded or uplifted by components of compressional stress, rather than solely undergoing reverse-motion slip along high-angle faults. Apparent normal displacements observed in the Quaternary sediment can result from localized areas of tension (or transtension) that occur in a transpressional fault zone, out-of-plane effects, and/or tensile stresses resulting from compressional uplift of the bedrock and soil.

Carbon-14 dating of displaced horizons indicated movement between approximately 26,000 and 42,000 YBP. The imaged structures represent the only known primary coseismic deformation of the Late Quaternary within the WVFS, and are considered “capable” structures by U.S. Army Corps of Engineers and Nuclear Regulatory Commission regulations.

The style and timing of deformation within the WVFS, the close association of soil faults to documented Pennsylvanian bedrock faults (Hovey Lake fault and Wabash Island fault), and focal mechanisms in the Wabash Valley seismic zone are all evidence that the extensionally formed Paleozoic faults of the WVFS have been reactivated in the Late Quaternary.

DISSEMINATION OF RESULTS

Woolery, E., 2005, Geophysical and geological evidence of neotectonic deformation along the Hovey Lake fault, Lower Wabash Valley Fault System, Central United States: **Bulletin of the Seismological Society of America**, v. 95, no. 3, 1193–1201.

Vance, D., Woolery, E., and VanArsdale, R. 2005, Coring Geophysical Anomalies: Towards Neotectonic Constraint Along the Hovey Lake Fault, Lower Wabash Valley Fault System: **77th Annual Meeting of the Eastern Section of the Seismological Society of America**, October 2–4, 2005, Memphis, TN.

Rutledge, F., Woolery, E., and Wang, Z., 2005, Geophysical and Geological Evidence of Neotectonic Deformation along the Hovey Lake Fault, Lower Wabash Valley Fault System, Central United States: **Seismological Research Letters**, 76, 1, p.116

Woolery, E., Rutledge, F., Wang, Z., 2004, Geophysical and Geological Evidence of Neotectonic Deformation Along the Hovey Lake Fault, Lower Wabash Valley Fault System, Central United States: **Eos Transactions AGU***, 85*(46), Fall Meet. Suppl., Abstract S53C-06

Rutledge, F., Woolery, E., Wang, Z., 2003, High-Resolution Geophysical Investigation of Late Quaternary Deformation in the Lower Wabash Valley Fault System, Central United States: **Eos Transactions AGU***, 84*(47), Fall Meet. Suppl., Abstract S21F-0402

ACKNOWLEDGEMENTS

In addition to the U.S. Geological Survey, Department of the Interior, NEHRP award number 04HQGR0094, the Kentucky Geological Survey (KGS) and the U.S. Army Corps of Engineers provided significant assistance to the investigation. The PIs wish to thank Drs. Zhenming Wang (KGS) and Ron Street (KGS), as well as, Messrs David Vance, Ting-Li Lin, William Reid, Steve McDowell, and Steve Wood for their considerable field efforts. They are also grateful to Meg Smath (KGS) and Collie Rulo (KGS) for editorial and graphic arts improvements to the report.

BIBLIOGRAPHY

Ault, C.H., Harper, D., Smith, C.R., and Wright, M.A., 1985, Faulting and jointing in and near surface mines of southwest Indiana: U.S. Nuclear Regulatory Commission Report NUREG/CR-4117, 27 p.

Ault, C.H., and Sullivan, D.M., 1982, Faulting in southwest Indiana: U.S. Nuclear RegulatoryCommission Report NUREG/CR-2908, 50 p.

Baker, G.S., 1999, Processing near-surface seismic-reflection data: A primer: Society of Exploration Geophysicists, Course Notes Series No. 9, p. 77.

Bear, G.W., Rupp, J.A., and Rudman, A.J., 1997, Seismic interpretation of the deep structure of the Wabash Valley Fault System: Seismological Research Letters, v. 68, no. 4, p. 624–640.

Black, R.A., Steeples, D.W., and Miller, R.D., 1994, Migration of shallow seismic reflection data: Geophysics, v. 59, no. 3, p. 402–410.

Braile, L.W., Hinze, W.J., and Keller, G.R., 1997, New Madrid seismicity, gravity anomalies, and interpreted ancient rift structures: Seismological Research Letters, v. 68, no. 4, p. 599–610.

Braile, L.W., Hinze, W.J., Keller, G.R., Lidiak, E.G., and Sexton, J.L., 1986, Tectonic development of the New Madrid rift complex, Mississippi Embayment, North America: Tectonophysics, v. 131, nos. 1–2, p. 1–21.

Braile, L.W., Keller, G.R., Hinze, W.J., and Lidiak, E.G., 1982, An ancient rift complex and its relation to contemporary seismicity in the New Madrid seismic zone: Tectonics, v. 1, p. 225–237.

Bristol, H.M., and Treworgy, J.D., 1979, The Wabash Valley fault system in southeastern Illinois: Illinois State Geological Survey Circular 509.

FMSM Engineers, 2002, Final Report – J.T. Myers Locks and Dam Seismological Study.

Harris, J.B., 1996, Shear-wave splitting in Quaternary sediments: Neotectonic implications in the New Madrid seismic zone: Geophysics, v. 61, p. 1871–1882.

Harris, J.B., Berman, S.A., Beard, W.C., Street, R.L., and Cox, R.T., 1998, Shallow seismic reflection investigations of neotectonic activity in the Lower Mississippi Valley: Society of Exploration Geophysicists, Expanded Abstracts.

Harrison, R.W., and Schultz, A., 1994, Strike-slip faulting at Thebes Gap, Missouri and Illinois: Implications for New Madrid tectonism: Tectonics, v. 13, p. 246–257.

Harrison, R., Hoffman, D., Vaughn, J., Palmer, J., Wiscombe, C., McGeehin, J., Stephenson, W., Odum, J., Williams, R., and Forman, S., 1999, An example of neotectonism in a continental interior—Thebes Gap, Midcontinent United States: Tectonophysics, v. 305, p. 399–417.

Hildenbrand, T.G., and Hendricks, J.D., 1995, Geophysical setting of the Reelfoot Rift and relations between rift structures and the New Madrid seismic zone, *in* Investigations of the New Madrid seismic zone, Shedlock, K., and Johnston, A., eds.: U.S. Geological Survey Professional Paper 1538-E, p. 1–30.

Hildenbrand, T.G., Kane, M.F., and Hendricks, J.D., 1982, Magnetic basement in the upper Mississippi Embayment region-A preliminary report, *in* Investigations of the New Madrid, Missouri, earthquake region, Pakiser, L., and McKeown, F.A., eds.: U.S. Geological Survey Professional Paper 1236-E, p. 39–53.

Hildenbrand, T.G., McBride, J.H., and Ravat, D., 2002, The Commerce geophysical lineament and its possible relation to Mesoproterozoic igneous complexes and large earthquakes in the central Illinois Basin: Seismological Research Letters, v. 73, no. 5, p. 640–659.

Hildebrand, T.G., and Ravat, D., 1997, Geophysical setting of the Wabash Valley fault system: Seismological Research Letters, v. 68, no. 4, p. 567–585.

Kim, W.Y., 2003, The 18 June 2002 Caborn, Indiana, earthquake: Reactivation of ancient rift in the Wabash Valley seismic zone?: Bulletin of Seismological Society of America, v. 93, no. 5, p. 2201–2211.

Kolata, D.R., and Nelson, W.J., 1991, Tectonic history of the Illinois Basin, *in* Interior cratonic basins, Leighton, M.W., Kolata, D.R., Oltz, D.F., and Eidel, J.J., eds.: American Association of Petroleum Geologists Memoir 51, p. 263–285.

Langenheim, V.E., and Hildenbrand, T.G., 1994, Gravity and magnetic study of the Arkansas to Illinois lineament-A northeast-trending feature parallel to the Reelfoot graben [abs.]: Eos, Transactions, American Geophysical Union, v. 75, p. 580.

Langenheim, V.E., and Hildenbrand, T.G., 1997, The Commerce geophysical lineament—its source, geometry, and relation to the Reelfoot Rift and New Madrid seismic zone: Geological Society of America Bulletin, v. 109, no. 5, p. 580–595.

McBride, J.H., Sargent, M.L., and Potter, C.J., 1997, Investigation Possible Earthquake-Related Structure Beneath the Southern Illinois Basin from Seismic Reflection: Seismological Research Letters, v. 68, n. 4, p. 641–649.

Munson, P.J., Obermeier, S.F., Munson, C.A., and Hajic, E.R., 1997, Liquefaction evidence for Holocene and latest Pleistocene seismicity in the southern halves of Indiana and Illinois; a preliminary overview: Seismological Research Letters, v. 68, no. 4, p. 521–536.

Nelson, W.J. and Bauer, R.A., 1987, Thrust faults in southern Illinois basin: Result of contemporary stress?: Geological Society of America Bulletin, v. 98, p. 302–307.

Nelson, W.J., and Lumm, D.K., 1987, Structural geology of southeastern Illinois and vicinity: Illinois State Geological Survey Circular 538, 70 p.

Obermeier, S.F., 1998, Liquefaction evidence for strong earthquakes of Holocene and latest Pleistocene ages in the states of Indiana and Illinois, USA: Engineering Geology, v. 50, nos. 3–4, p. 227–254.

Odum, J.K., Stephenson, W.J., Shedlock, K.M., and Pratt, T.L., 1998, Near-surface structural model for deformation associated with the February 7, 1812, New Madrid, Missouri, earthquake: Geological Society of America Bulletin, v. 110, no. 2, p. 149–162.

Pond, E.C., and Martin, J.R., 1997, Estimated magnitudes and accelerations associated with prehistoric earthquakes in the Wabash Valley region of the central United States: Seismological Research Letters, v. 68, no. 4, p. 611–623.

Rene, R.M., and Stanonis, F.L., 1995, Reflection seismic profiling of the Wabash Valley fault system in the Illinois Basin: USGS Professional Paper 1538-O, 33 p.

Roberts, M.T., 1983, Seismic example of complex faulting from northwest shelf of Palawan, Philippines, *in* A Picture and Work Atlas—Seismic expressions of structural style, Bally, A.W., ed.: American Assoication of Petroleum Geologists, v. 3, p. 4.2-18–4.2-21.

Rudman, A.J., Pavlis, G.L., Hamburger, M.W., and Pope, B.M., 1997, A comprehensive geophysical investigation to assess seismic hazards in the Wabash Valley seismic zone: A case study of the New Harmony fault: USGS-NEHRP Final Technical Report, 14 p.

Schweig, E.S., Shen, F., Kanter, L.R., Luzietti, E.A., VanArsdale, R.B., Shedlock, K.M., and King, K.W., 1992, Shallow seismic reflection survey of the Bootheel lineament area, southeastern Missouri: Seismological Research Letters, v. 63, p. 285–295.

Sexton, J.L., and Jones, P.B., 1986, Evidence of recurrent faulting in the New Madrid seismic zone from mini-Sosie high-resolution reflection data: Geophysics, v. 51, p. 1760–1788.

Sheriff, R.E., 1977, Limitations on Resolution of Seismic Reflections and Geologic Detail Derivable from them: in Payton, C.E., editor, Seismic Stratigraphy—Applications to Hydrocarbon exploration: American Association of Petroleum Geologists, Memoir 26, p. 3-14.

Sheriff, R.E., Geldart, L.P., 1989, Exploration Seismology Vol. 1: History, Theory, and Data Acquisition: Cambridge, Cambridge University Press, 244 p.

Stephenson, W.J., Odum, J.K., Williams, R.A., Pratt, T.L., Harrison, R.W., and Hoffman, D., 1999, Deformation and Quaternary faulting in southeast Missouri across the Commerce geophysical lineament: Bulletin of the Seismological Society of America, v. 89, p. 140–155.

Street, R., Bollinger, G., and Woolery, E., 2002, Blasting and other mining-related activities in Kentucky—A source of earthquake misidentification: Seismological Research Letters, v. 73, no. 5, p. 739–750.

Taylor, K.B., Herrmann, R.B., Hamburger, M.W., Pavlis, G.L, Johnston, A., Lager, C., and Lam, C., 1989, The southeastern Illinois earthquake of 10 June 1987: Seismological Research Letters, v. 60, no. 3, p. 101–109.

Thomas, W.A., 1993, Low-angle detachment geometry of the late Precambrian–Cambrian Appalachian-Ouachita rifted margin of southeastern North America: Geological Society of America Bulletin, v. 103, p. 415–431.

Treworgy, J.D., 1981, Structural features in Illinois—A Compendium: Illinois State Geological Survey Circular 519, 22 p.

Wheeler, R.L., 1997, Boundary separating the seismically active Reelfoot Rift from the sparsely seismic Rough Creek Graben, Kentucky and Illinois: Seismological Research Letters, v. 68, no. 4, p. 586–598.

Wheeler, R.L., and Ravat D., 2002, Introduction: Seismicity, Quaternary Faulting, and Seismic Hazard: Seismological Research Letters, v. 73, no. 5, p. 590–596.

Williams, R.A., Luzietti, E.A., and Carver, D.L., 1995, High-resolution seismic imaging of Quaternary faulting on the Crittenden County fault zone, New Madrid seismic zone, northeastern Arkansas: Seismological Research Letters, v. 66, p. 42–57.

Woolery, E.W., Street, R.L., Wang, Z., and Harris, J.B., 1993, Near-surface deformation in the New Madrid seismic zone as imaged by high-resoultion SH-wave seismic methods: Geophysical Research Letters, v. 20, n. 15, p. 1615–1618.

Woolery, E.W., and Street, R.L., 2002, Quaternary fault reactivation in the Fluorspar Area fault complex of western Kentucky: Evidence from shallow SH-wave reflection profiles: Seismological Research Letters, v. 73, p. 628–639.

Woolery, E.W., Wang, Z., Street, R.L., and Harris, J.B., 1996, A P-and SH-wave seismic reflection investigation of the Kentucky Bend scarp in the New Madrid seismic zone: Seismological Research Letters, v. 66, no. 2, p. 67–74.

Zoback, M.L., and Zoback, M., 1980, State of stress in the conterminous United States: Journal of Geophysical Research, v. 85, no. B11, p. 6113–6156.